Aerodynamic Computations Using The Convective Upstream Split Pressure Scheme With Local Preconditioning

by

Marian Nemec

A thesis submitted in conformity with the requirements
for the degree of Master of Applied Science
Graduate Department of Aerospace Science and Engineering
University of Toronto

Abstract

Aerodynamic Computations Using
The Convective Upstream Split Pressure Scheme
With Local Preconditioning

Marian Nemec
Master of Applied Science
Graduate Department of Aerospace Science and Engineering
University of Toronto
1998

The implementation of the convective upstream split pressure (CUSP) approach to numerical dissipation is presented for an approximately-factored algorithm in conjunction with time-derivative local preconditioning. Two different 'soft' flux limiters, one of which is new, are used to to blend the low and high order CUSP dissipation in order to enforce monotonic solutions. The resulting algorithm is applied to several turbulent aerodynamic flows and compared with results obtained using scalar and matrix numerical dissipation models. The results show the CUSP scheme to be very effective in providing good shock capturing, low numerical dissipation in boundary layers, and low numerical errors in drag. The two flux limiters provide equivalent accuracy; however, a reduction in computational cost was obtained with the newly proposed 'soft' limiter. Overall, the CUSP scheme is competitive with matrix dissipation in terms of accuracy at a reduced cost. For flows with Mach number below 0.2, convergence is significantly accelerated with the preconditioned algorithm, and the preconditioned CUSP scheme is superior to the preconditioned scalar scheme and the original CUSP scheme.

Acknowledgements

I would like to thank the following individuals who made significant contributions to this research:

- Prof. Zingg for excellent supervision and guidance.
- Dr. Raw for insightful discussions.
- Stan De Rango for his invaluable help with SC1, Jason Lassaline for his LaTeX expertise, and our system administrator Mike Sullivan.
- My friends and the staff at UTIAS for providing a warm and enjoyable atmosphere for the pursuit of my studies.
- My family for their support and understanding.

Joint funding from AEA Technology, Advanced Scientific Computing, and the Natural Sciences and Engineering Research Council of Canada is gratefully acknowledged. This research was also supported by an OGS scholarship from the Government of Ontario.

Marian Nemec

University of Toronto
March 30, 1998

Contents

List of Tables

List of Figures

List of Symbols

A, B	flux Jacobian matrices
$\hat{A}, \hat{B}$	derivation form of flux Jacobian matrices
CFL	Courant number
E, F	curvilinear convective flux vectors
$\widehat{E}, \widehat{F}$	Cartesian convective flux vectors
J	metric Jacobian
M	transfer matrix
M	Mach Number
Pr	Prandtl number
Q	curvilinear state vector
$\hat{Q}$	derivation form of state vector
Re	Reynolds number
S	viscous flux vector
T	eigenvector matrix
U, V	contravariant velocities

c	speed of sound
e	total energy
p	pressure
u, v	Cartesian velocities
Δt	time step
x, y	physical (Cartesian) coordinates

Λ	eigenvalue matrix
Γ	preconditioner
γ	specific heat ratio
ϵ	preconditioning parameter
ε	limiter parameter
λ	eigenvalue
μ	molecular viscosity
ξ, η	curvilinear coordinates
ρ	density
σ	spectral radius

Chapter 1

Introduction

Successful computational methods for the solution of the Navier-Stokes and Euler equations must meet numerous requirements. The algorithms should be robust, accurate, computationally inexpensive, and provide a fast turn-around. High resolution of shock waves, contact discontinuities, and boundary layers free of overshoot and oscillation is desired. One area which plays a significant role in attaining these goals is numerical dissipation.

The concept of numerical dissipation is based on wave interactions which cause the creation of high and low frequency waves in the medium. In real fluids, the high frequency waves are damped out by the fluid's viscosity. Unfortunately, when the Euler equations are used to model the flow, the equations are by definition inviscid, and therefore, there is no mechanism present to damp out the high frequency waves. The high frequencies build up and cause instability, poor accuracy, and poor convergence characteristics. Hence some form of numerical dissipation (also referred to as artificial dissipation or artificial viscosity) must be added to the algorithm. Even in the Navier-Stokes equations, numerical dissipation is required since outside of the boundary layer the flow is essentially inviscid. Further, present day grid resolution is not sufficient to provide appropriate viscosity throughout the computational domain.

Many modern viscous solvers for compressible flows, such as ARC2D [1], use second-order centered differences for the spatial discretization of the governing equations. The advantages of centered differences are that they are more efficient and relatively easy to implement when compared to upwind schemes. Upwind schemes use concepts from characteristic theory to determine the direction of the 'wind' and then proceed to apply appropriate

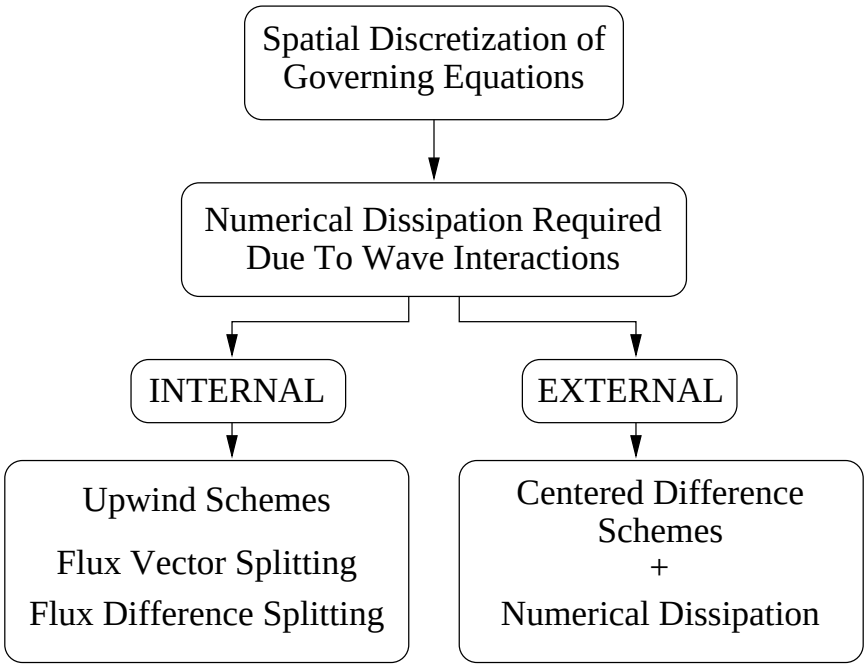

Figure 1.1: Numerical dissipation and spatial discretization.

one-sided spatial differences. The one-sided differences are dissipative, and consequently, for these schemes the numerical dissipation is inherent in the formulation. The user, therefore, has only very limited control over the dissipation. However, when centered differences are used for the spatial discretization, it is necessary to explicitly include some form of numerical dissipation in order to obtain the correct solution, as shown in Fig. 1.1.

There are numerous dissipation schemes available for use with centered differences, but presently each scheme has some undesirable properties, such as poor accuracy in certain regions of the flow or high demand on computational power. Recently the Convective Upstream Split Pressure (CUSP) scheme has been introduced, which has the potential to eliminate most of these undesirable properties. The purpose of this work is to present a detailed evaluation of the CUSP scheme in the context of aerodynamic flows.

1.1 Literature Review

The most widely used technique for numerical dissipation for centered differences is referred to as scalar dissipation. A popular nonlinear scalar scheme was first introduced

in the early 1980s by Jameson, Schmidt, and Turkel [2] (sometimes called the JST scheme), and it has proven to be successful for a wide range of CFD applications. The scheme is easy to implement and requires minimal computational effort. Unfortunately, accuracy and shock resolution problems occur when scalar dissipation is used. Allmaras [3] found that scalar dissipation contaminates boundary layers, resulting in non-physical solutions within the boundary layer. Reddy and Papadakis [4] reported that overdissipation in viscous flow leads to poor drag predictions. These problems are attributed to the fact that the spectral radius of the convective flux Jacobian matrix is used as a measure of the dissipation levels needed.

The performance of the scalar scheme for low Mach number flow was improved with the development of local preconditioning. Unrau and Zingg [5] implemented the local time-derivative preconditioning of Weiss and Smith [6], and obtained significant improvements in both accuracy and convergence. The use of the preconditioned spectral radius in the scalar scheme reduces the excessive dissipation within the boundary layers.

For transonic flow, the problems of scalar dissipation were reduced with upwind schemes and matrix dissipation, but with a corresponding increase in computational effort per grid node. In the late 1980s, Swanson and Turkel [7] introduced matrix dissipation where the flux Jacobian matrix is used to scale the dissipation. Turkel [8] developed a special form of the flux Jacobian to reduce the operations count for the matrix-vector evaluation. The reduced dissipation in boundary layers produced improved accuracy, especially for drag predictions. Turkel and Vatsa [9] applied matrix dissipation to 3-D calculations and reported that matrix dissipation outperformed scalar dissipation in terms of accuracy for a given grid.

Frew and Zingg [10] implemented matrix dissipation in the approximately-factored algorithm ARC2D [1]. Their conclusions were that 1) the additional cost of matrix dissipation is 35% over scalar dissipation, 2) matrix dissipation is successful at reducing the contribution of artificial dissipation to the overall flux balance with little effect on convergence rate, and 3) for flow cases dominated by friction drag, matrix dissipation leads to substantial reduction in grid density. However, for high lift cases, where pressure drag is dominant, the use of matrix dissipation is unjustified.

Both Swanson and Turkel [7], and Frew and Zingg [10] observed that shock capturing of the matrix scheme was superior to the scalar scheme. Frew and Zingg [10] implemented the original pressure switch used by Jameson, Schmidt, and Turkel [2] in the scalar

scheme and noted minor oscillations upstream and downstream of the shock. Swanson and Turkel [7] modified the original pressure switch to include flux limiters based on pressure which preserve monotonicity of the solution. They obtained oscillation-free shocks equivalent to upwind schemes. Unfortunately, the use of flux limiters may cause a stall in the convergence rate after the residual has been reduced by few orders of magnitude. Venkatakrishnan [11] addressed this problem with the development of 'soft limiters' which converge to steady state. In 1993, Jameson [12] introduced a new class of limiter functions which add anti-diffusive terms to the first-order scheme. These limiters preserve monotonicity of the solution and are sensitive to the changes in all conservative variables. Jameson [12] also incorporated the 'soft limiters' of Venkatakrishnan [11] and obtained good convergence rates.

In 1995, Jameson [12, 13] presented the Convective Upstream Split Pressure (CUSP) scheme, a high-resolution scheme for compressible viscous flows with shocks. CUSP belongs to a family of schemes based on a splitting of the flux vector into convective and pressure flux contributions. Another scheme which uses flux splitting is the Advection Upstream Splitting Method (AUSM) introduced by Liou and Steffen [14], which has recently been implemented in conjunction with local preconditioning by Edwards and Liou [15].

The CUSP scheme is specifically developed for oscillation-free, single-interior-point shock capturing, and also provides low dissipation for low Mach numbers. The formulation of the scheme does not require evaluation of a matrix-vector product, which saves on computational effort. Tatsumi, Martinelli, and Jameson [16] have presented skin friction and shock capturing results which appear very promising. Two versions of the CUSP scheme have been introduced, ECUSP and HCUSP, where HCUSP is formulated to conserve stagnation enthalpy.

In 1997, Swanson, Radespiel, and Turkel [17] studied the HCUSP scheme and concluded that 1) for transonic viscous flow and coarser meshes, the accuracy in aerodynamic coefficients is better with the matrix scheme than with the CUSP scheme, and 2) the CUSP scheme requires 40% more computer time than the scalar scheme, while the matrix scheme needs about 15% more time. They noted that the poorer accuracy may be due to unwanted limiter activation, while the excessive computer time is due to evaluating the limiter for each conservative equation. For comparison, the pressure switch requires only one evaluation.

Tweedt, Chima, and Turkel [18] implemented the CUSP scheme into a preconditioned solver for 3-D viscous flow around turbomachine blade rows. They observed a

significant improvement in accuracy over the preconditioned scalar scheme.

This literature review briefly summarizes the development of numerical dissipation schemes for centered differences. Although some research work has been done with the CUSP scheme, a detailed study of the scheme for viscous aerodynamic computations is lacking. The issues addressed in this thesis are outlined in the following section.

1.2 Project Definition and Objectives

The objective of this thesis is to investigate the practical use of the ECUSP numerical dissipation scheme introduced by Jameson [12, 13] for viscous aerodynamic computations. The goals are subdivided as follows:

1. Implement the scheme in the implicit, approximately-factored solver SC1 [19] and compare the results with the scalar and matrix dissipation schemes.

2. For low Mach number flow, implement the scheme in conjunction with local preconditioning and compare the results with the preconditioned scalar scheme.

Factors under consideration include dissipation in boundary layers, shock capturing, drag prediction, effect on convergence, and cost per node. The overriding goal is to decrease the number of grid nodes required to obtain lift and drag coefficients of a given accuracy at a reasonable cost per node, thus reducing the overall computational expense.

Chapter 2

Governing Equations and Numerical Method

The solver used to investigate the various numerical dissipation schemes is SC1 [19], which is based on the Navier-Stokes solver ARC2D [1]. The flow of air around the airfoils of interest is modeled by the Navier-Stokes equations. Since these flows are characterized by high Reynolds number viscous flows, the governing equations are reduced to the thin-layer Navier-Stokes equations. This chapter describes the methodology of SC1.

2.1 Thin-Layer Navier-Stokes Equations

The two-dimensional thin-layer Navier-Stokes equations, written in generalized curvilinear coordinates, are:

$$\frac{\partial Q}{\partial t} + \frac{\partial E}{\partial \xi} + \frac{\partial F}{\partial \eta} = \mathrm{Re}^{-1} \frac{\partial S}{\partial \eta} \tag{2.1}$$

where,

$$Q = J^{-1} \begin{bmatrix} \rho \\ \rho u \\ \rho v \\ e \end{bmatrix} \tag{2.2}$$

The convective flux vectors are

$$E = J^{-1} \begin{bmatrix} \rho U \\ \rho U u + \xi_x p \\ \rho U v + \xi_y p \\ (e+p)U - \xi_t p \end{bmatrix} \tag{2.3}$$

$$F = J^{-1} \begin{bmatrix} \rho V \\ \rho V u + \eta_x p \\ \rho V v + \eta_y p \\ (e+p)V - \eta_t p \end{bmatrix} \tag{2.4}$$

with

$$U = \xi_t + \xi_x u + \xi_y v, \quad V = \eta_t + \eta_x u + \eta_y v \tag{2.5}$$

the contravariant velocities. The variable J represents the metric Jacobian of the transformation:

$$J^{-1} = (x_\xi y_\eta - x_\eta y_\xi) \tag{2.6}$$

The viscous flux vector is

$$S = J^{-1} \begin{bmatrix} 0 \\ \eta_x m_1 + \eta_y m_2 \\ \eta_x m_2 + \eta_y m_3 \\ \eta_x (u m_1 + v m_3 + m_4) \\ +\eta_y (u m_2 + v m_3 + m_5) \end{bmatrix} \tag{2.7}$$

with

$$\begin{aligned} m_1 &= \mu(4\eta_x u_\eta - 2\eta_y v_\eta)/3 \\ m_2 &= \mu(\eta_y u_\eta + \eta_x v_\eta) \\ m_3 &= \mu(-2\eta_x u_\eta + 4\eta_y v_\eta)/3 \\ m_4 &= \mu \mathcal{P}r^{-1}(\gamma-1)^{-1}\eta_x \partial_\eta(a^2) \\ m_5 &= \mu \mathcal{P}r^{-1}(\gamma-1)^{-1}\eta_y \partial_\eta(a^2) \end{aligned} \tag{2.8}$$

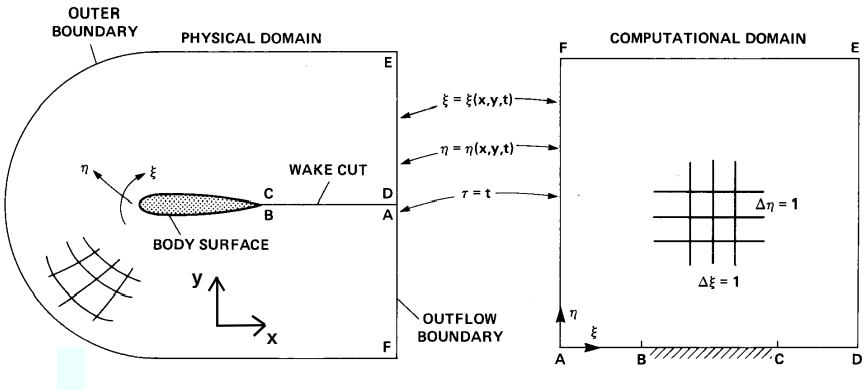

Figure 2.1: Curvilinear coordinate transformation (used with permission from T. H. Pulliam)

Pressure is related to the conservative flow variables, Q, by the equation of state for a perfect gas, as follows

$$p = (\gamma - 1)\left(e - \frac{1}{2}\rho(u^2 + v^2)\right) \tag{2.9}$$

The thin-layer Navier-Stokes equations are derived in the generalized coordinate system (ξ, η) in order to facilitate the use of curvilinear 'C' grids. The airfoils of interest are characterized by smooth curved sections. Therefore, the grids which are used to discretize the physical domain around the airfoil are constructed such that the grid lines follow the contours of the airfoil in one direction and are perpendicular to the airfoil in the other direction. These directions are referred to as ξ and η respectively. A transformation is used to map the grid into a rectangular computational domain as illustrated in Fig. 2.1.

2.2 Numerical Method

We are interested only in the steady-state solution of the governing equations outlined in section 2.1. Therefore, it is sufficient to use a first-order time-marching method to advance the solution to steady state. SC1 [19] uses the first-order implicit Euler method since it has a broad stability region. When the implicit Euler time-marching scheme is

applied to Eq. 2.1 one obtains,

$$Q^{n+1} - Q^n + \Delta t \left(\partial_\xi E^{n+1} + \partial_\eta F^{n+1} - \mathrm{Re}^{-1} \partial_\eta S^{n+1} \right) = 0 \tag{2.10}$$

where Δt is the time step and $Q^n = Q(n\Delta t)$. The vectors E, F, and S are locally linearized,

$$\begin{aligned} E^{n+1} &= E^n + A^n \Delta Q^n + O(\Delta t^2) \\ F^{n+1} &= F^n + B^n \Delta Q^n + O(\Delta t^2) \\ S^{n+1} &= S^n + K^n \Delta Q^n + O(\Delta t^2) \end{aligned} \tag{2.11}$$

where $\Delta Q = Q^{n+1} - Q^n$, and the matrices A, B, and K are the flux Jacobians, defined by

$$A = \tfrac{\partial E}{\partial Q},\ B = \tfrac{\partial F}{\partial Q}, \text{ and } K = \tfrac{\partial S}{\partial Q}.$$

Approximate factorization [1] is introduced in order to avoid the direct inversion of the sparse matrix formed on the left-hand-side. Note that the modifications to the left-hand-side may impact the convergence rate of the solver, but they do not affect the steady-state solution of the problem. Combining Eq. 2.11 with approximate factorization, and substituting into Eq. 2.10 gives,

$$[I + \Delta t \delta_\xi A^n][I + \Delta t \delta_\eta B^n - \Delta t \mathrm{Re}^{-1} \delta_\eta K^n] \Delta Q^n = R^n \tag{2.12}$$

where

$$R^n = -\Delta t [\delta_\xi E(Q^n) + \delta_\eta F(Q^n) - \mathrm{Re}^{-1} \delta_\eta S(Q^n)]$$

The symbol δ in Eq. 2.12 denotes a complete spatial operator, including the numerical dissipation. Central differences are used for the spatial discretization, which requires the explicit addition of numerical dissipation (see chapter 3).

To further reduce the complexity of the left-hand-side, the diagonal form [1] is implemented. The Jacobian matrices are diagonalized as follows,

$$\Lambda_\xi = T_\xi^{-1} A T_\xi \tag{2.13}$$

$$\Lambda_\eta = T_\eta^{-1} B T_\eta \tag{2.14}$$

where the matrices Λ_ξ and Λ_η are diagonal matrices whose elements are the eigenvalues of the flux Jacobians. The eigenvalue matrices also contain a contribution from the viscous

flux Jacobian [1]. The matrix T_ξ has the eigenvectors of A as columns, and T_η has the eigenvectors of B as columns. The eigenvector matrices are factored out, giving

$$T_\xi[I + \Delta t \delta_\xi \Lambda_\xi] T_\xi^{-1} T_\eta [I + \Delta t \delta_\eta \Lambda_\eta] T_\eta^{-1} \Delta Q^n = R^n \tag{2.15}$$

Variable time stepping is used to accelerate the convergence rate by roughly equalizing the Courant numbers of each cell. Since the grids used have highly stretched cells, the majority of the Courant number variation may be eliminated by scaling with the Jacobian:

$$\Delta t = \frac{\Delta t_{ref}}{1 + \sqrt{J}} \tag{2.16}$$

Boundary conditions are imposed on the surface of the airfoil and at the outer boundary of the mesh. The no-slip condition is enforced at the body, while Riemann invariants are applied at the outer boundary [1]. The effects of turbulence are modeled by the Baldwin-Lomax turbulence model [1].

2.3 Local Preconditioning

Local preconditioning is implemented in SC1 in order to increase the accuracy of the solver and accelerate the convergence rate for low Mach number flows [5]. The eigenvalues of the flux Jacobian matrices A and B, given in Eq. 2.11, are $U, U, U \pm c\sqrt{{\xi_x}^2 + {\xi_y}^2}$ and $V, V, V \pm c\sqrt{{\eta_x}^2 + {\eta_y}^2}$, respectively, where c is the speed of sound. The convergence rate of the solver depends on the magnitude and the nature of these eigenvalues. At low Mach numbers, the eigenvalues have significantly differing magnitudes resulting in poor convergence rates. The local preconditioning matrix Γ is introduced in order to bring the magnitudes of the eigenvalues closer together as follows,

$$\Gamma \frac{\partial Q}{\partial t} + \frac{\partial E}{\partial \xi} + \frac{\partial F}{\partial \eta} = \mathrm{Re}^{-1} \frac{\partial S}{\partial \eta} \tag{2.17}$$

This time-derivative preconditioning destroys the time accuracy of the system, but at steady state, $\frac{\partial Q}{\partial t} = 0$, and hence, the steady-state solution should be unaffected as long as both Γ and Γ^{-1} exist. Writing the inviscid terms in quasi-linear form and premultiplying by Γ^{-1} gives

$$\frac{\partial Q}{\partial t} + \Gamma^{-1} A \frac{\partial Q}{\partial \xi} + \Gamma^{-1} B \frac{\partial Q}{\partial \eta} = \mathrm{Re}^{-1} \Gamma^{-1} \frac{\partial S}{\partial \eta} \tag{2.18}$$

Thus the preconditioned flux Jacobians are $\Gamma^{-1}A$ and $\Gamma^{-1}B$. With a suitable choice of Γ, the spread of the eigenvalues of the preconditioned flux Jacobians can be substantially reduced.

In order to simplify the form of the preconditioning matrix, the following symmetry variables are used

$$\partial\hat{Q} = J^{-1}\begin{bmatrix} \frac{1}{\rho c}\partial p \\ \partial u \\ \partial v \\ \partial p - c^2\partial\rho \end{bmatrix} \tag{2.19}$$

The symmetry variables are related to the conservative variables through the following transfer matrices

$$M = \begin{bmatrix} \frac{\rho}{c} & 0 & 0 & -\frac{1}{c^2} \\ \frac{\rho u}{c} & \rho & 0 & -\frac{u}{c^2} \\ \frac{\rho v}{c} & 0 & \rho & -\frac{v}{c^2} \\ \rho\left(\frac{u^2+v^2}{2c} + \frac{c}{\gamma-1}\right) & \rho u & \rho v & -\frac{u^2+v^2}{2c^2} \end{bmatrix} \tag{2.20}$$

$$M^{-1} = \begin{bmatrix} (\gamma-1)\frac{u^2+v^2}{2\rho c} & (1-\gamma)\frac{u}{\rho c} & (1-\gamma)\frac{v}{\rho c} & \frac{\gamma-1}{\rho c} \\ -\frac{u}{\rho} & \frac{1}{\rho} & 0 & 0 \\ -\frac{v}{\rho} & 0 & \frac{1}{\rho} & 0 \\ \frac{\gamma-1}{2}\left(u^2+v^2\right) - c^2 & (1-\gamma)u & (1-\gamma)v & (\gamma-1) \end{bmatrix} \tag{2.21}$$

which are derived from

$$M = \frac{\partial Q}{\partial\hat{Q}},\ M^{-1} = \frac{\partial\hat{Q}}{\partial Q} \tag{2.22}$$

The local preconditioning matrices and the flux Jacobians in the two variable sets are related by

$$\Gamma = M\hat{\Gamma}M^{-1} \tag{2.23}$$

$$A = M\hat{A}M^{-1} \tag{2.24}$$

$$B = M\hat{B}M^{-1} \tag{2.25}$$

Thus a local preconditioner formulated in terms of the symmetry variables is applied to the thin-layer Navier-Stokes equations written in terms of the conservative variables as follows

$$M\hat{\Gamma}M^{-1}\frac{\partial Q}{\partial t} + \frac{\partial E}{\partial\xi} + \frac{\partial F}{\partial\eta} = \mathrm{Re}^{-1}\frac{\partial S}{\partial\eta} \tag{2.26}$$

Similarly, the diagonal form of the algorithm, Eq. 2.15, can be written in terms of the eigenvectors of the preconditioned flux Jacobians. The diagonal form of the algorithm becomes:

$$M\hat{\Gamma}\hat{T}_{\xi,\Gamma}\left[I+\Delta t\delta_\xi\Lambda_{\xi,\Gamma}\right]\hat{T}^{-1}_{\xi,\Gamma}\hat{T}_{\eta,\Gamma} \left[I+\Delta t\partial_\eta(\Lambda_{\eta,\Gamma}-\mathrm{Re}^{-1}N_\eta)\right]\hat{T}^{-1}_{\eta,\Gamma}M^{-1}\Delta Q = R^n \quad (2.27)$$

where the subscript Γ indicates the preconditioned system, and $\Lambda_{\kappa,\Gamma}$ is a diagonal matrix containing the eigenvalues of $\hat{\Gamma}^{-1}\hat{A}$ and $\hat{\Gamma}^{-1}\hat{B}$ with $\kappa=\xi$ and η, respectively, and R^n is defined in Eq. 2.12. The term N_η is a diagonal contribution from the viscous terms which is defined later.

The preconditioner of Weiss and Smith [6] is used for the time-derivative preconditioning in SC1. When written in terms of the symmetry variable, the preconditioner has a particularly simple form:

$$\hat{\Gamma}=\begin{bmatrix}\frac{1}{\epsilon}&0&0&0\\0&1&0&0\\0&0&1&0\\0&0&0&1\end{bmatrix},\ \hat{\Gamma}^{-1}=\begin{bmatrix}\epsilon&0&0&0\\0&1&0&0\\0&0&1&0\\0&0&0&1\end{bmatrix} \quad (2.28)$$

where ϵ is chosen as follows,

$$\epsilon=\min\left[1,\max\left(\mathrm{M}^2,\epsilon_1,\epsilon_2\right)\right] \quad (2.29)$$

With $\epsilon=\mathrm{M}^2$, where M is the local Mach number, the Weiss-Smith preconditioner provides effective low Mach number preconditioning. However, ϵ must remain finite in stagnation regions. To this end, a lower limit is placed on ϵ based on the freestream Mach number:

$$\epsilon_1=\phi\mathrm{M}^2_\infty \quad (2.30)$$

where ϕ is a free parameter, and for most flows can be set to one. In addition, the following lower limit is sometimes imposed:

$$\epsilon_2=\chi\frac{\mu_\infty\sqrt{\max\left(\xi_x^2+\xi_y^2,\eta_x^2+\eta_y^2\right)}}{\rho u_\infty} \quad (2.31)$$

where χ is the second free parameter associated with the preconditioner. This prevents the preconditioned pseudo-acoustic velocities from becoming too small relative to the local diffusion velocity, $\nu/\Delta x$.

Lastly, ϵ is chosen such that $\epsilon = 1$ for Mach numbers greater than one. Thus the preconditioner reduces to the identity matrix for supersonic flows, and the original system of equations is recovered. This feature also allows backward compatibility with the unpreconditioned equations.

With this preconditioner, the following eigenvalue matrices are obtained:

$$\Lambda_{\kappa,\Gamma} = \begin{bmatrix} U_\kappa & 0 & 0 & 0 \\ 0 & U_\kappa & 0 & 0 \\ 0 & 0 & \lambda_{\kappa,+} & 0 \\ 0 & 0 & 0 & \lambda_{\kappa,-} \end{bmatrix} \tag{2.32}$$

where U_κ denotes the contravariant velocity in ξ or η direction. The eigenvalues $\lambda_{\kappa,\pm}$ are

$$\lambda_{\kappa,\pm} = \frac{1}{2}(1+\epsilon)U_\kappa \pm \frac{1}{2}\sqrt{(\epsilon-1)^2 U_\kappa^2 + 4\epsilon\left(\kappa_x^2+\kappa_y^2\right)c^2} \tag{2.33}$$

The eigenvector matrices, $\hat{T}_{\kappa,\Gamma}$, are:

$$\hat{T}_{\kappa,\Gamma} = \begin{bmatrix} 0 & 0 & \frac{\lambda_{\kappa,+}-U_\kappa}{\bar{\kappa}c} & \frac{U_\kappa-\lambda_{\kappa,-}}{\bar{\kappa}c} \\ 0 & \tilde{\kappa}_y & \tilde{\kappa}_x & -\tilde{\kappa}_x \\ 0 & -\tilde{\kappa}_x & \tilde{\kappa}_y & -\tilde{\kappa}_y \\ 1 & 0 & 0 & 0 \end{bmatrix} \tag{2.34}$$

where $\tilde{\kappa} = \kappa/\bar{\kappa}$ and $\bar{\kappa} = \sqrt{2(\kappa_x^2+\kappa_y^2)}$ with $\kappa = \xi$ or η. Finally, the contribution from the viscous terms is approximated by

$$N_\eta = k_{\mathrm{ARC2D}} \begin{bmatrix} 1 & 0 & 0 & 0 \\ 0 & 1 & 0 & 0 \\ 0 & 0 & \beta+\frac{\epsilon+1}{2} & 0 \\ 0 & 0 & 0 & -\beta+\frac{\epsilon+1}{2} \end{bmatrix} \tag{2.35}$$

where k_{ARC2D} is the scalar term used in ARC2D, and

$$\beta = \frac{(\epsilon-1)^2 U_\eta}{2\sqrt{(1-\epsilon)^2 U_\eta^2 + 4\epsilon(\eta_x^2+\eta_y^2)c^2}} \tag{2.36}$$

The far-field boundary conditions are modified to reflect the characteristic variables of the preconditioned system. The approach of Barth is used; for details see [5]. The local

time step is chosen based on the preconditioned eigenvalues to exploit the gains of local preconditioning. This leads to the following definition of Δt [5]:

$$\Delta t = \min \left[\frac{\rho}{\mu_\infty \max\left(\xi_x^2 + \xi_y^2, \eta_x^2 + \eta_y^2\right)}, \mathrm{CFL} \times \max\left(\frac{1}{\sigma_\xi}, \frac{1}{\sigma_\eta}\right) \right] \tag{2.37}$$

where σ_ξ and σ_η represent the preconditioned spectral radius, and CFL is user specified.

Chapter 3

Numerical Dissipation Models

The central differences used for spatial discretization of the governing equations require explicit numerical dissipation. The first three sections of this chapter describe three numerical dissipation models: the scalar, matrix, and CUSP schemes. In the final section, the scalar and CUSP schemes are modified so that they are implemented in conjunction with local preconditioning.

3.1 Scalar Dissipation Model

The nonlinear scalar numerical dissipation model developed by Jameson *et al.* [2] is added to a second-order centered-difference spatial operator in the following manner:

$$\delta_\xi E_{j,k} = \frac{E_{j+1,k} - E_{j-1,k}}{2\Delta\xi} - \nabla_\xi D_1 D_2 \tag{3.1}$$

with

$$\begin{aligned}
D_1 &= 2\sigma_{j+\frac{1}{2},k} J^{-1}_{j+\frac{1}{2},k} \\
D_2 &= \epsilon^{(2)}_{j+\frac{1}{2},k} \Delta_\xi J_{j,k} Q_{j,k} - \epsilon^{(4)}_{j+\frac{1}{2},k} \Delta_\xi \nabla_\xi \Delta_\xi J_{j,k} Q_{j,k} \\
\sigma_{j,k} &= |U| + c\sqrt{\xi_x^2 + \xi_y^2} \\
\epsilon^{(2)}_{j,k} &= \kappa_2 \max(\Upsilon_{j+1,k}, \Upsilon_{j,k}, \Upsilon_{j-1,k}) \\
\epsilon^{(4)}_{j,k} &= \max(0, \kappa_4 - \epsilon^{(2)}_{j,k}) \\
\Upsilon_{j,k} &= \frac{|p_{j+1,k} - 2p_{j,k} + p_{j-1,k}|}{|p_{j+1,k} + 2p_{j,k} + p_{j-1,k}|}
\end{aligned}$$

where Δ_ξ and ∇_ξ are first-order forward and backward difference operators, U is a contravariant velocity component, and κ_2 and κ_4 are constants. Typical values of κ_2 and κ_4 are 1.0 and 0.01 respectively. The scalar coefficient σ is the spectral radius of A, the flux Jacobian matrix given by $\partial E/\partial Q$. The term $\Upsilon_{j,k}$ is a pressure switch to control the use of first-order dissipation near shock waves. An analogous term appears in the η direction.

On the left-hand-side of the implicit approximately-factored algorithm, the contribution from the dissipation is added to the diagonal entries.

3.2 Matrix Dissipation Model

The matrix dissipation model is based on that of Swanson and Turkel [7]. The term D_1 in Eq. 3.1 becomes

$$D_1 = |A|_{j+\frac{1}{2},k} J^{-1}_{j+\frac{1}{2},k} \tag{3.2}$$

where

$$|A| = T_\xi |\Lambda_\xi| T_\xi^{-1} \tag{3.3}$$

The columns of T_ξ are the right eigenvectors of A and

$$|\Lambda_\xi| = \begin{bmatrix} |U| & 0 & 0 & 0 \\ 0 & |U| & 0 & 0 \\ 0 & 0 & |U + c\sqrt{\xi_x^2 + \xi_y^2}| & 0 \\ 0 & 0 & 0 & |U - c\sqrt{\xi_x^2 + \xi_y^2}| \end{bmatrix} \tag{3.4}$$

In the present implementation the pressure switch is retained for sensing shocks. The shock capturing capabilities can be improved through the use of more complex flux limiters which can incorporate TVD (Total Variation Diminishing) properties [7]. Again the terms in the η direction are analogous. The treatment of the left-hand-side is similar to scalar dissipation.

Near stagnation points and sonic points, some of the eigenvalues of A approach zero. In order to avoid the problems this may introduce, the elements of $|\Lambda_\xi|$ are modified as follows:

$$\begin{aligned} \tilde{\lambda}_1, \tilde{\lambda}_2 &= \max(\lambda_{1,2}, V_l \sigma) \\ \tilde{\lambda}_3 &= \max(\lambda_3, V_n \sigma) \\ \tilde{\lambda}_4 &= \max(\lambda_4, V_n \sigma) \end{aligned} \tag{3.5}$$

V_l and V_n can be set to zero for subsonic flows, but finite values are needed for transonic flows. Commonly used values are $V_l = 0.025$ and $V_n = 0.25$, but for some cases values as high as 0.3 are required.

The matrix scheme requires the evaluation of the matrix-vector product $|A|\Delta Q$ which adds considerable computational expense over the scalar scheme. A direct method of evaluating the matrix-vector product [8] is implemented in the algorithm in order to reduce the expense.

3.3 CUSP Dissipation Model

The CUSP [12, 13] scheme is formulated by a combination of differences of the state and flux vectors. Two different CUSP schemes have been developed, HCUSP and ECUSP. HCUSP conserves stagnation enthalpy for steady flows and was studied by Swanson *et al.* [17]. In this study only the ECUSP version is considered, and for the remainder of this study ECUSP is referred to as the CUSP scheme. The scheme is implemented in conjunction with the SLIP limiter [12]. Specific details pertaining to the implementation of the CUSP scheme in the solver SC1 [19] are outlined in Appendix C. To better understand the implementation of the scheme in SC1, the scheme is first introduced for the 1-D Euler equations.

3.3.1 CUSP Fundamentals in 1-D

Consider the 1-D Euler equations written in semi-discrete form

$$\Delta x \frac{dq_j}{dt} + h_{j+\frac{1}{2}} - h_{j-\frac{1}{2}} = 0 \tag{3.6}$$

where q_j is the state vector $\begin{pmatrix} \rho & \rho u & e \end{pmatrix}^T$, and $h_{j+\frac{1}{2}}$ is the numerical flux between nodes j and $j+1$. The numerical flux is given by

$$h_{j+\frac{1}{2}} = \frac{1}{2}\left(f_{j+1} + f_j\right) - d_{j+\frac{1}{2}} \tag{3.7}$$

where

$$f = \begin{bmatrix} \rho \\ \rho u^2 + p \\ u\left(e + p\right) \end{bmatrix} \tag{3.8}$$

and d is the numerical dissipation vector. Note that this representation gives a central difference formulation for the spatial discretization of the fluxes, plus a dissipative term at node j given by $d_j = d_{j+\frac{1}{2}} - d_{j-\frac{1}{2}}$.

A general form of the numerical dissipation vector can be written as

$$d_{j+\frac{1}{2}} = \nu_{j+\frac{1}{2}} B_{j+\frac{1}{2}} \left(q_{j+1} - q_j\right) + \phi_{j+\frac{1}{2}} \left(f_{j+1} - f_j\right) \tag{3.9}$$

The scalar scheme described in section 3.1 is obtained from Eq. 3.9 by setting $B_{j+\frac{1}{2}} = \sigma_{j+\frac{1}{2}}$, where σ is the spectral radius of the flux Jacobian, $\phi_{j+\frac{1}{2}} = 0$, and $\nu_{j+\frac{1}{2}}$ is a user selected scaling factor. Matrix dissipation is obtained by setting $B_{j+\frac{1}{2}} = \left|A_{j+\frac{1}{2}}\right|$ and $\phi_{j+\frac{1}{2}} = 0$. Note that the numerical dissipation given in Eq. 3.9 is only first-order accurate unless appropriate anti-dissipative terms are introduced which is discussed in section 3.3.3.

The CUSP scheme is obtained from Eq. 3.9 by rewriting it in the following form

$$d_{j+\frac{1}{2}} = \frac{1}{2}\alpha^{\star}_{j+\frac{1}{2}} c \left(q_{j+1} - q_j\right) + \frac{1}{2}\beta_{j+\frac{1}{2}} \left(f_{j+1} - f_j\right) \tag{3.10}$$

where c represents the local speed of sound, and $\alpha^{\star}$ and β are scalar coefficients. Thus, the scheme is a linear combination of the state and flux vectors and does not contain any matrix-vector products. The coefficients $\alpha^{\star}$ and β are chosen such that the CUSP scheme satisfies the following criteria:

1. Obtain shock structures with a single interior point.

2. Introduce enough dissipation to ensure stability, but do not pollute the solution with excessive dissipation.

Jameson [12] shows that a single-point stationary shock is obtained by numerical dissipation schemes which:

1. Produce a first-order upwind flux for supersonic flow.

2. Satisfy a generalized eigenvalue problem for the exit from the shock of the form

$$\left(A_{AR} + \alpha_{AR} B_{AR}\right)\left(q_R - q_A\right) = 0 \tag{3.11}$$

where the subscript A denotes a state within the shock, and subscript R denotes the state downstream of the shock.

For supersonic flows, choosing the coefficients $\alpha^{\star}_{j+\frac{1}{2}} = 0$ and $\beta_{j+\frac{1}{2}} = sign(M)$, the CUSP scheme with the centered-difference spatial operator becomes a first-order upwind scheme. Next, the coefficients are chosen to satisfy the generalized eigenvalue problem. For flows where $0 \leq M \leq 1$, the following expression is obtained when the left and right flux vectors are in equilibrium at the exit from a stationary shock

$$A_{AR}\left(q_R - q_A\right) = -\frac{\alpha^{\star}_{j+\frac{1}{2}} c}{1+\beta_{j+\frac{1}{2}}}\left(q_R - q_A\right) \tag{3.12}$$

The eigenvalues of A_{AR}, the flux Jacobian matrix, are u, $u+c$, and $u-c$. Since flows with $u > 0$ require positive dissipation, the eigenvalue $u-c$ is selected. Thus, the coefficients $\alpha^{\star}$ and β are related by

$$-\frac{\alpha^{\star} c}{1+\beta} = u - c \tag{3.13}$$

Rearranging for $\alpha^{\star}$, the following relation is obtained

$$\alpha^{\star} = (1+\beta)(1-M) \tag{3.14}$$

For a flow region where $-1 \leq M \leq 0$, Eq. 3.14 becomes

$$\alpha^{\star} = (1-\beta)(1+M) \tag{3.15}$$

With Eq. 3.14 and Eq. 3.15, the CUSP scheme meets the criteria for a single interior point shock structure. Coefficient β is now selected to fulfill the second criterion regarding the accuracy of the dissipation scheme.

First, it should be noted that the flux vector f consists of two physically distinct parts, namely convective and pressure terms:

$$f = u\begin{pmatrix}\rho\\ \rho u\\ e\end{pmatrix} + \begin{pmatrix}0\\ p\\ up\end{pmatrix} = uq + f_p \tag{3.16}$$

The convective terms are transported by the flow velocity, while the pressure flux terms are governed by the acoustic wave speeds [14]. Jameson [13] defines the total effective coefficient of convective dissipation (α) as

$$\alpha c = \alpha^{\star} c + \beta \bar{u} \tag{3.17}$$

where $\bar{u}$ is the arithmetic mean flow velocity. Eq. 3.17 is obtained by splitting the flux terms in Eq. 3.10 and collecting the terms containing the state vector.

For low dissipation near stagnation points and within boundary layers select $\alpha c = \bar{u}$. This choice also leads to smooth upwinding since the dissipation is continuous across a sonic line. Combining Eq. 3.14, Eq. 3.15, and Eq. 3.17, the β coefficient becomes

$$\beta = \begin{cases} \max\left(0, \frac{\overline{u}+\lambda^-}{\overline{u}-\lambda^-}\right) & \text{if } 0 \leq M \leq 1 \\ -\max\left(0, \frac{\overline{u}+\lambda^+}{\overline{u}-\lambda^+}\right) & \text{if } -1 \leq M < 0 \\ \text{sign}(M) & \text{if } |M| > 1 \end{cases} \tag{3.18}$$

where

$$\lambda^{\pm} = u \pm c$$

The Roe average is used to determine u and c, and thus $M = u/c$.

The 'max' function in Eq. 3.18 forces β to equal zero when the local Mach number is less than 0.5, in order to prevent the dissipation from becoming anti-dissipative. Without the 'max' function, β would be less than zero when $M < 0.5$, which could cause stability problems. Hence, for Mach numbers below 0.5, the CUSP scheme is a scalar scheme with Mach number scaling. Note that when $\beta = 0$, the CUSP scheme does not satisfy the generalized eigenvalue problem given in Eq. 3.11 at the exit from a shock. Consequently, oscillation-free, one-point shock structures are not attainable when the exit Mach number is below 0.5. It is important to realize that Eq. 3.17 should be used to determine $\alpha^\star$ rather than Eqs. 3.14 and 3.15.

Swanson *et al.* [17] point out that the β function could be modified such that even stronger shocks are captured properly. For example, if $\alpha c = 2\bar{u}$ then $\beta = \max(0, (2\bar{u} + \lambda^-)/(\bar{u} - \lambda^-))$ which would allow one point shock capturing for shock exit Mach number of 1/3. However, in practical aerodynamic flows, shocks with exit Mach numbers less than 0.5 are rare. For example, the test cases studied in chapter 4 indicate that this modification is not necessary. Further, defining $\alpha c = 2\bar{u}$ means that for flow regions when $\beta = 0$, the dissipation is twice the original amount which may overdissipate the boundary layer.

Lastly, Jameson [13] suggests that near stagnation points it is sometimes necessary to modify α such that $\alpha = \frac{1}{2}\left(\alpha_0 + \frac{M^2}{\alpha_0}\right)$ when $|M|$ is smaller than α_0. This modification may be necessary when solving the Euler equations in regions where $\bar{u} \approx 0$, but for the thin-layer Navier-Stokes equations it was not required.

The coefficients $\alpha^\star$ and β have now been chosen such that both the shock capturing and accuracy criteria are satisfied. Unlike the scalar and matrix schemes, the first-order CUSP scheme has no user selected parameters. The choice of $\alpha^\star$ and β allows capturing of oscillation-free shocks with one interior point, but the CUSP scheme is not a total-variation-diminishing (TVD) scheme. The following section examines the TVD properties of the CUSP scheme when applied to the 1-D Euler equations.

3.3.2 Is CUSP TVD?

To explore TVD or LED (Local Extremum Diminishing) [12] properties of the CUSP scheme, introduce a characteristic decomposition and assume frozen Jacobians. Roe linearization is used to write the CUSP scheme (Eq. 3.10) in the following form:

$$d_{j+\frac{1}{2}} = T\mathcal{M}_{j+\frac{1}{2}}T^{-1}\left(q_{j+1} - q_j\right) \tag{3.19}$$

where $\mathcal{M}$ is a diagonal matrix with eigenvalues $\mu_1 c$, $\mu_2 c$, and $\mu_3 c$ given by

$$\begin{aligned}
\mu_1 &= |M| \\
\mu_2 &= \begin{cases} |M| & \text{if } |M| < \frac{1}{2} \\ \alpha + \beta & \text{if } \frac{1}{2} \le |M| \le 1 \\ |M+1| & \text{if } |M| > 1 \end{cases} \\
\mu_3 &= \begin{cases} |M| & \text{if } |M| < \frac{1}{2} \\ \alpha - \beta & \text{if } \frac{1}{2} \le |M| \le 1 \\ |M-1| & \text{if } |M| > 1 \end{cases}
\end{aligned}$$

Sub Eq. 3.19 into Eq. 3.6 to obtain the following semi-discrete form:

$$\begin{aligned}
\frac{dq_j}{dt} = -\frac{1}{2\Delta x}\Big(&A_{j+\frac{1}{2}}\Delta q_{j+\frac{1}{2}} + A_{j-\frac{1}{2}}\Delta q_{j-\frac{1}{2}} \\
&- T\mathcal{M}_{j+\frac{1}{2}}T^{-1}\Delta q_{j+\frac{1}{2}} + T\mathcal{M}_{j-\frac{1}{2}}T^{-1}\Delta q_{j-\frac{1}{2}}\Big)
\end{aligned} \tag{3.20}$$

where

$$\Delta q_{j+\frac{1}{2}} = q_{j+1} - q_j$$

Diagonalize the flux Jacobians in Eq. 3.20 and factor to obtain,

$$\frac{dq_j}{dt} = \frac{1}{2\Delta x}\left[T\left(\mathcal{M}_{j+\frac{1}{2}} - \Lambda_{j+\frac{1}{2}}\right)T^{-1}\Delta q_{j+\frac{1}{2}} - T\left(\Lambda_{j-\frac{1}{2}} + \mathcal{M}_{j-\frac{1}{2}}\right)T^{-1}\Delta q_{j-\frac{1}{2}}\right] \tag{3.21}$$

where Λ is a diagonal matrix with eigenvalues u, $u+c$, and $u-c$. In order for the CUSP scheme to satisfy the TVD criteria, both coefficients in front of the Δq's must be ≥ 0.

To test whether the CUSP scheme satisfies the TVD criteria consider the following examples: 1) subsonic flow with $0 < u < \frac{c}{2}$, 2) subsonic flow with $\frac{c}{2} \leq u \leq c$, and 3) supersonic flow with $u > c$. For case 1, the matrices in Eq. 3.21 become

$$\mathcal{M}_{j+\frac{1}{2}} - \Lambda_{j+\frac{1}{2}} = \begin{bmatrix} u & 0 & 0 \\ 0 & u & 0 \\ 0 & 0 & u \end{bmatrix} - \begin{bmatrix} u & 0 & 0 \\ 0 & u+c & 0 \\ 0 & 0 & u-c \end{bmatrix} = \begin{bmatrix} 0 & 0 & 0 \\ 0 & -c & 0 \\ 0 & 0 & c \end{bmatrix} \tag{3.22}$$

and

$$\mathcal{M}_{j-\frac{1}{2}} + \Lambda_{j-\frac{1}{2}} = \begin{bmatrix} 2u & 0 & 0 \\ 0 & 2u+c & 0 \\ 0 & 0 & 2u-c \end{bmatrix} \tag{3.23}$$

Thus, for subsonic flows with $M < 0.5$ the positivity of the coefficients in front of the characteristic variables is not satisfied, and consequently, the scheme is not TVD.

For case 2, where $\frac{c}{2} \leq u \leq c$, the following results are obtained,

$$\mathcal{M}_{j+\frac{1}{2}} - \Lambda_{j+\frac{1}{2}} = \begin{bmatrix} u & 0 & 0 \\ 0 & (\alpha+\beta)c & 0 \\ 0 & 0 & (\alpha-\beta)c \end{bmatrix} - \begin{bmatrix} u & 0 & 0 \\ 0 & u+c & 0 \\ 0 & 0 & u-c \end{bmatrix} = \begin{bmatrix} 0 & 0 & 0 \\ 0 & 2(u-c) & 0 \\ 0 & 0 & 2(c-u) \end{bmatrix} \tag{3.24}$$

and

$$\mathcal{M}_{j-\frac{1}{2}} + \Lambda_{j-\frac{1}{2}} = \begin{bmatrix} 2u & 0 & 0 \\ 0 & 4u & 0 \\ 0 & 0 & 0 \end{bmatrix} \tag{3.25}$$

Again, the scheme is not TVD. The coefficient for $\Delta q_{j+\frac{1}{2}}$ (Eq. 3.24) does not satisfy the positivity requirement, but the second coefficient (Eq. 3.25) remains positive in the selected Mach number range.

For the supersonic case 3, positivity is enforced for the corresponding characteristic variable as is shown below,

$$\mathcal{M}_{j+\frac{1}{2}} - \Lambda_{j+\frac{1}{2}} = \begin{bmatrix} u & 0 & 0 \\ 0 & u+c & 0 \\ 0 & 0 & u-c \end{bmatrix} - \begin{bmatrix} u & 0 & 0 \\ 0 & u+c & 0 \\ 0 & 0 & u-c \end{bmatrix} = 0 \tag{3.26}$$

and

$$\mathcal{M}_{j-\frac{1}{2}} + \Lambda_{j-\frac{1}{2}} = \begin{bmatrix} 2u & 0 & 0 \\ 0 & 2(u+c) & 0 \\ 0 & 0 & 2(u-c) \end{bmatrix} \tag{3.27}$$

Therefore, for this case the scheme is TVD as both coefficients are ≥ 0. This is expected since the coefficients $\alpha^\star$ and β were selected such that the scheme becomes a first-order upwind scheme for supersonic flow.

Consequences of the fact that the CUSP scheme is not TVD for subsonic flow are illustrated in Fig. 3.1. The figure shows the Mach number profile for a quasi 1-D flow through a duct with a sudden area change. The first-order CUSP scheme produces oscillations at the discontinuity, while with the first-order matrix and scalar schemes oscillation-free solutions are obtained. The matrix scheme captures the discontinuity particularly well, and both the CUSP and matrix schemes produce a more accurate solution downstream of the discontinuity due to lower dissipation. These results were obtained by setting the user selected coefficient $\kappa_2 = 1.0$ for both the scalar and matrix schemes.

In the next section, the CUSP scheme is implemented into SC1 [19]. Also, the CUSP scheme is expanded to obtain third-order dissipation in smooth regions of the flow. Appropriate flux limiter and anti-dissipation terms are added to the scheme.

3.3.3 SC1 and CUSP

The implementation of the CUSP scheme with SC1 follows directly from the concepts introduced in section 3.3.1 for 1-D. Special attention is given to Roe linearization and the curvilinear coordinates. For the ξ direction, the first-order CUSP scheme, given by Eq. 3.10, is modified as follows

$$d_{j+\frac{1}{2},k} = \frac{1}{2} J^{-1}_{j+\frac{1}{2},k} \alpha^\star_{j+\frac{1}{2},k} \left(\tilde{Q}_{j+1,k} - \tilde{Q}_{j,k} \right) + \frac{1}{2} J^{-1}_{j+\frac{1}{2},k} \beta_{j+\frac{1}{2}} \Delta E_{j+\frac{1}{2},k} \tag{3.28}$$

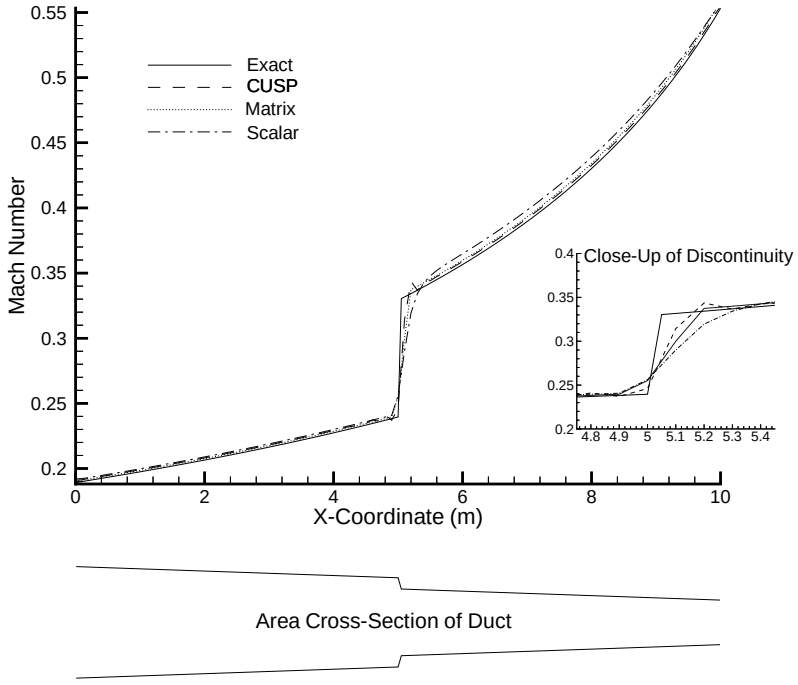

Figure 3.1: Subsonic flow through a tapered duct with a step area change.

where

$$\Delta E_{j+\frac{1}{2},k} = \xi_{x_{j+\frac{1}{2},k}} \left(\widehat{E}_{j+1,k} - \widehat{E}_{j,k} \right) + \xi_{y_{j+\frac{1}{2},k}} \left(\widehat{F}_{j+1,k} - \widehat{F}_{j,k} \right)$$

and $\tilde{Q} = J \cdot Q$. The metrics at the half nodes are evaluated with a simple average. The flux vectors $\widehat{E}$ and $\widehat{F}$ denote the flux vectors in Cartesian coordinates given by,

$$\widehat{E} = \begin{bmatrix} \rho u \\ \rho u^2 + p \\ \rho uv \\ u(e+p) \end{bmatrix} \tag{3.29}$$

$$\widehat{F} = \begin{bmatrix} \rho v \\ \rho vu \\ \rho v^2 + p \\ v(e+p) \end{bmatrix} \tag{3.30}$$

The parameters $\alpha^\star$ and β are given by

$$\alpha^\star = \left| \overline{U} \right| - \beta \overline{U} \tag{3.31}$$

$$\beta = \begin{cases} \max\left(0, \frac{\overline{U}+\lambda^-}{\overline{U}-\lambda^-}\right) & \text{if } 0 \le M \le 1 \\ -\max\left(0, \frac{\overline{U}+\lambda^+}{\overline{U}-\lambda^+}\right) & \text{if } -1 \le M < 0 \\ \text{sign}(M) & \text{if } |M| > 1 \end{cases} \tag{3.32}$$

where

$$\lambda^\pm = U \pm c\sqrt{\xi_x^2 + \xi_y^2}$$

Note that $\overline{U}$ is the arithmetic mean contravariant velocity, while the eigenvalues $\lambda^\pm$ are determined by Roe linearization.

To construct a higher-order CUSP scheme, limiters are added which activate near flow discontinuities. The purpose of a limiter is to blend first- and third-order dissipation in order to resolve flow discontinuities such as shock waves without oscillations yet maintain high accuracy of the solver in smooth regions of the flow. The pressure switch given in Eq. 3.1 is used for this purpose in the scalar and matrix schemes. Since the switch is only sensitive to pressure, it works fairly well for capturing discontinuities such as shocks, but

other discontinuities, such as a contact surface, are invisible to a pressure switch. In order to make the switch more universal and to improve its performance, Jameson [12] introduced the following family of SLIP (Symmetric Limited Positive) limiter functions

$$R(u,v) = 1 - \left| \frac{u-v}{|u|+|v|} \right|^q \tag{3.33}$$

where $q \geq 2$, and u and v are defined later. Various values of q were evaluated and good performance is obtained with $q = 2$.

A higher-order CUSP scheme is obtained by defining the limited average,

$$L(u,v) = \frac{1}{2} R(u,v)\,(u+v) \tag{3.34}$$

and then constructing the appropriate left and right states for each variable,

$$\begin{aligned} \tilde{Q}_L^{(n)} &= \tilde{Q}_j^{(n)} + \frac{1}{2} L\left(\Delta\tilde{Q}^{(n)}_{j+\frac{3}{2},k}, \Delta\tilde{Q}^{(n)}_{j-\frac{1}{2},k} \right) \\ \tilde{Q}_R^{(n)} &= \tilde{Q}_{j+1}^{(n)} - \frac{1}{2} L\left(\Delta\tilde{Q}^{(n)}_{j+\frac{3}{2},k}, \Delta\tilde{Q}^{(n)}_{j-\frac{1}{2},k} \right) \end{aligned} \tag{3.35}$$

where the superscript n represents the nth element of the state vector. Consequently, the dissipative flux becomes

$$d_{j+\frac{1}{2},k} = \frac{1}{2} J^{-1}_{j+\frac{1}{2},k} \alpha^{\star}_{j+\frac{1}{2},k} \left(\tilde{Q}_{R,k} - \tilde{Q}_{L,k} \right) + \frac{1}{2} J^{-1}_{j+\frac{1}{2},k} \beta_{j+\frac{1}{2}} \Delta E(\tilde{Q}_{R,L_{j+\frac{1}{2},k}}) \tag{3.36}$$

where

$$\Delta E(\tilde{Q}_{R,L_{j+\frac{1}{2},k}}) = \xi_{x_{j+\frac{1}{2},k}} \left(\widehat{E}(\tilde{Q}_{R,k}) - \widehat{E}(\tilde{Q}_{L,k}) \right) + \xi_{y_{j+\frac{1}{2},k}} \left(\widehat{F}(\tilde{Q}_{R,k}) - \widehat{F}(\tilde{Q}_{L,k}) \right) \tag{3.37}$$

An analogous term appears in the η direction.

The scalar and matrix schemes presented in sections 3.1 and 3.2 use two coefficients, κ_2 and κ_4, which are user selected. Comparison of the scalar scheme with the CUSP scheme reveals that for CUSP similar 'effective' coefficients can be obtained. For CUSP, $\kappa_2 = \frac{1}{2}$ in order to obtain upwinding in supersonic flow. To obtain κ_4, take out the factor of $\frac{1}{2}$ from Eq. 3.34 which forces $\kappa_4 = \kappa_2 \cdot \frac{1}{2} = \frac{1}{4}$. For the scalar scheme $\kappa_4 = 2 \cdot 0.01 = 0.02$, which is significantly smaller than the CUSP scheme. Further, note that the dissipation is scaled by $|M+1|c$ for the scalar scheme compared to $|M|c$ for the CUSP scheme. Thus, at low Mach numbers (i.e. near a solid surface), CUSP is less dissipative than the scalar scheme, and see section 3.4.2 for further discussion regarding the impact of the coefficients.

The function of the coefficient κ_4 is only to provide sufficient dissipation for stability. Therefore, the dependence of κ_4 on κ_2 in the CUSP scheme is not desirable. Swanson *et al.* [17] introduce a free parameter which scales the third-order CUSP dissipation independent of κ_2. The parameter modifies the limited average as follows,

$$L(u,v,w) = \frac{1}{2}R(u,w)\left[(1-\kappa_4)\,v + \kappa_4\frac{(u+w)}{2}\right] \tag{3.38}$$

with the new left and right states determined by

$$\begin{aligned}
\tilde{Q}_L^{(n)} &= \tilde{Q}_j^{(n)} + \frac{1}{2}L\left(\Delta\tilde{Q}^{(n)}_{j+\frac{3}{2},k}, \Delta\tilde{Q}^{(n)}_{j+\frac{1}{2},k}, \Delta\tilde{Q}^{(n)}_{j-\frac{1}{2},k}\right) \\
\tilde{Q}_R^{(n)} &= \tilde{Q}_{j+1}^{(n)} - \frac{1}{2}L\left(\Delta\tilde{Q}^{(n)}_{j+\frac{3}{2},k}, \Delta\tilde{Q}^{(n)}_{j+\frac{1}{2},k}, \Delta\tilde{Q}^{(n)}_{j-\frac{1}{2},k}\right)
\end{aligned} \tag{3.39}$$

If $\kappa_4 = 1$ the original scheme is obtained. The advantage of the new parameter is that it can potentially increase the accuracy of CUSP. The possible disadvantages are that the coefficient may be case sensitive and selecting inappropriate values may result in divergence of the solver. Swanson *et al.* [17] note that for values of κ_4 below $\frac{1}{4}$ convergence problems occur.

The action of the limiter given in Eq. 3.33 is illustrated in Fig. 3.2. Near a flow discontinuity, u and v have opposite signs and therefore $R(u,v) \to 0$. In smooth regions of the flow $R(u,v) \to 1$, which provides third-order dissipation. A problem with this limiter function is that it is insensitive to the relative magnitudes of u and v, as is shown in Fig. 3.2b. In near constant regions of the flow field, small fluctuations in u and v can trigger the limiter randomly, which may stall the convergence of the solution. One way to overcome this difficulty is to freeze the limiter once the convergence rate stalls. A better approach is suggested by Jameson [12], who follows the work of Venkatakrishnan [11]. The limiter function is modified as follows,

$$R(u,v) = 1 - \left|\frac{u-v}{\max\left(|u|+|v|\,,(\varepsilon\Delta x)^{\frac{3}{2}}\right)}\right|^q \tag{3.40}$$

where

$$\Delta x = \sqrt{x_\xi^2 + x_\eta^2}$$

This 'soft limiter' introduces a threshold below which first-order dissipation is not activated, and therefore, triggering of the limiter for small extrema does not occur. For inappropriate

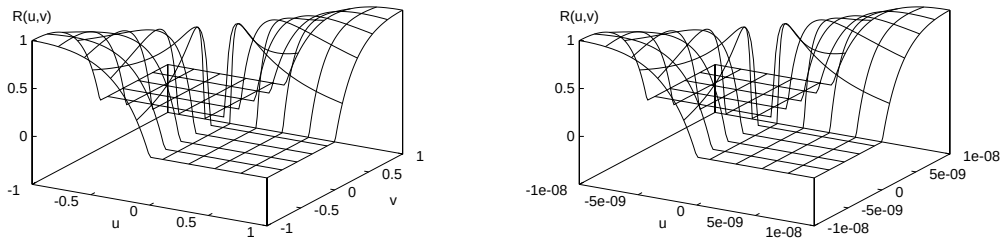

(a) Large differences in u and v.

(b) Small differences in u and v.

Figure 3.2: Jameson's original limiter function.

values of ε, the resulting threshold may be too high, and consequently, visible oscillations may develop around discontinuities. Venkatakrishnan [11] suggests values for ε between 1.0 and 5.0. The value of $\varepsilon = 5.0$ produces successful results, and this limiter is referred to as the V limiter.

We also modified Eq. 3.33 to create a new limiter which is shown below,

$$R(u,v) = 1 - \left| \frac{u - v}{|u| + |v| + \frac{\varepsilon}{|u|+|v|}} \right|^q \tag{3.41}$$

In this case, the parameter ε controls the activation of the limiter. For transonic flows, appropriate values for ε are between 10^{-2} to 10^{-4}, the smaller the value, the more first-order dissipation is used. Best results are obtained with $\varepsilon = 10^{-3}$. This limiter is referred as the Z limiter. Note that this limiter requires less expense than the V limiter.

On the left-hand-side of the implicit approximately factored algorithm, we use the diagonal form. The eigenvalues associated with the CUSP scheme, which are given in Eq. 3.19, and the appropriate limiter values are added to the diagonal entries.

3.4 Local Preconditioning and Numerical Dissipation

Unrau and Zingg [5] showed that two significant improvements were made with the preconditioned algorithm: 1) faster convergence, and 2) increased accuracy for low Mach number flow. In order to realize these gains the numerical dissipation should be

modified to reflect the preconditioned system of equations. The following section briefly explains the modifications to the scalar scheme, and this chapter concludes by explaining the preconditioned CUSP algorithm.

3.4.1 Preconditioned Scalar Scheme

The flux Jacobians of the preconditioned system are $\Gamma^{-1}A$ and $\Gamma^{-1}B$. Consequently, the spectral radius of the preconditioned flux Jacobian is used for scaling the dissipation scheme as follows,

$$\delta_\xi E_{j,k} = \frac{E_{j+1,k} - E_{j-1,k}}{2\Delta\xi} - \nabla_\xi D_1 D_2 \tag{3.42}$$

where

$$\begin{aligned} D_1 &= 2\sigma_{j+\frac{1}{2},k}\Gamma_{j+\frac{1}{2},k}J^{-1}_{j+\frac{1}{2},k} \\ \sigma_{j,k} &= \frac{1}{2}(1+\epsilon)\left|U_\xi\right| + \frac{1}{2}\sqrt{(\epsilon-1)^2U_\xi^2 + 4\epsilon\left(\xi_x^2+\xi_y^2\right)c^2} \end{aligned}$$

with the remaining variables unchanged from Eq. 3.1, and ϵ is defined in Eq. 2.29. Note that the preconditioned spectral radius is a function of $\left(\Gamma^{-1}A\right)$, and therefore, the multiplication by Γ in the term D_1 is necessary in order to be consistent with the flux vector E. On the left-hand-side, the preconditioned spectral radii are used in place of the original spectral radii.

The difficulties associated with the scalar model, such as the excessive dissipation in the boundary layer, are greatly reduced with the preconditioned spectral radius. In low speed flow, the acoustic velocity dominates the original spectral radius and causes excessive dissipation, which scales with $|M+1|c$. The preconditioned spectral radius does not have this problem, and the scaling is proportional to $|M|c$.

Before introducing the preconditioned CUSP dissipation scheme, it is insightful to closely examine the effect of multiplying the dissipation vector by the matrix Γ. In order to simplify the analysis, we use the 1-D Euler equations defined in section 3.3.1. The order of magnitude of the elements in the Γ matrix, state vector, and flux vector is expressed in terms of ϵ. Recall that effective low Mach number preconditioning is obtained with $\epsilon = M^2$.

The entries in the Γ matrix in terms of the order of ϵ are

$$\Gamma = M\hat{\Gamma}M^{-1} = \begin{bmatrix} 0(1) & 0\left(\epsilon^{-\frac{1}{2}}\right) & 0\left(\epsilon^{-1}\right) \\ 0(\epsilon) & 0\left(1\right) & 0\left(\epsilon^{-\frac{1}{2}}\right) \\ 0(1) & 0\left(\epsilon^{-\frac{1}{2}}\right) & 0\left(\epsilon^{-1}\right) \end{bmatrix} \tag{3.43}$$

For low Mach number flows, the changes in the state vector scale with ϵ as follows,

$$\Delta q = \begin{bmatrix} \Delta\rho \\ \Delta\rho u \\ \Delta e \end{bmatrix} = \begin{bmatrix} 0(\epsilon) \\ 0\left(\epsilon^{\frac{1}{2}}\right) \\ 0(\epsilon) \end{bmatrix} \tag{3.44}$$

Thus, the product $\Gamma\Delta q$ becomes

$$\Gamma\Delta q = \begin{bmatrix} 0(1) \\ 0\left(\epsilon^{\frac{1}{2}}\right) \\ 0(1) \end{bmatrix} \tag{3.45}$$

The order of magnitude for the preconditioned spectral radius is $0(\epsilon^{\frac{1}{2}})$. Therefore, the first-order scalar dissipation can be expressed in terms of the order of ϵ as follows,

$$\sigma\Gamma\Delta q = \begin{bmatrix} 0\left(\epsilon^{\frac{1}{2}}\right) \\ 0\left(\epsilon\right) \\ 0\left(\epsilon^{\frac{1}{2}}\right) \end{bmatrix} \tag{3.46}$$

The same relation is also obtained for the CUSP scheme.

The order of the dissipation vector should be the same as the flux vector. This is indeed the case, since the order of magnitude for the flux vector is

$$\Delta f = \begin{bmatrix} \Delta\rho u \\ \Delta(\rho u^2 + p) \\ \Delta u(e + p) \end{bmatrix} = \begin{bmatrix} 0\left(\epsilon^{\frac{1}{2}}\right) \\ 0\left(\epsilon\right) \\ 0\left(\epsilon^{\frac{1}{2}}\right) \end{bmatrix} \tag{3.47}$$

Hence the scaling on the dissipation terms is consistent with the scaling on the flux terms. It is interesting to note that if there is no premultiplication by Γ then

$$\sigma\Delta q = \begin{bmatrix} 0\left(\epsilon^{\frac{3}{2}}\right) \\ 0\left(\epsilon\right) \\ 0\left(\epsilon^{\frac{3}{2}}\right) \end{bmatrix} \tag{3.48}$$

In this case, the mass and energy conservation equations may not have enough dissipation which could cause poor convergence.

3.4.2 Preconditioned CUSP Scheme

Unrau and Zingg [5] show that local preconditioning is most effective for flows with freestream Mach numbers below 0.3. In this region, the CUSP scheme reduces to scalar dissipation, with the scaling proportional to $|M|c$. Swanson *et al.* [17] note that with this scaling, CUSP dissipation is well suited for local preconditioning, since a similar scaling is used by the preconditioned scalar scheme, provided that the dissipation is augmented by the preconditioning matrix.

Therefore, the first-order CUSP scheme for the preconditioned algorithm is given by

$$d_{j+\frac{1}{2},k} = \frac{1}{2}\alpha^{\star}_{j+\frac{1}{2},k}\Gamma_{j+\frac{1}{2},k}J^{-1}_{j+\frac{1}{2},k}\left(Q_{j+1,k} - Q_{j,k}\right) \tag{3.49}$$

where

$$\alpha^{\star} = \bar{U}$$

Higher-order CUSP scheme is constructed as outlined in section 3.3.3. Tweedt *et al.* [18] obtain $\bar{U}$ from the left and right states given by Eqs. 3.39. In the present work, the arithmetic mean is used to compute $\bar{U}$. Both V and Z limiters can be used with the scheme; however, the subsonic test case studied did not require these limiters. Note that the multiplication by the preconditioner Γ is necessary to ensure appropriate scaling of the dissipation for the mass and energy equations, as the analysis in section 3.4.1 reveals.

Lastly, it is interesting to compare the magnitude of the user-selected coefficient of the preconditioned scalar scheme with the 'effective' coefficient of the preconditioned CUSP scheme. For CUSP dissipation, the third-order coefficient consists of the following contributions: $\frac{1}{2}$ from Eq. 3.49, $\frac{1}{2}$ from the implementation of the anti-diffusive terms (Eq. 3.34), and the user-selected value of κ_4. In the present work, $\kappa_4 = 1$ is generally used to ensure good convergence, hence the effective coefficient premultiplying $\bar{U}$ is $\frac{1}{4}$. For the preconditioned scalar scheme, the factor of 0.02 is the same as obtained in section 3.3.3. However, in the limit of $\epsilon \to 0$, the preconditioned spectral radius adds a factor of $\frac{1}{2}\left(1+\sqrt{5}\right)$, and therefore, the scaling coefficient for the scalar scheme becomes 0.03. Although the coefficient of the scalar scheme is smaller than the CUSP coefficient, the results indicate that the CUSP scheme introduces far less dissipation. This is due to the fact that for grids with cells which are reasonably aligned with the flow, $\alpha^{\star}$ is smaller in the normal direction when

compared with the preconditioned spectral radius of the scalar scheme, where ϵ is based on the flow Mach number. This is also true for the original CUSP and scalar schemes, since the contribution of the spectral radius is large in both ξ and η directions for the scalar scheme due to the presence of the speed of sound.

Chapter 4

Results and Discussion

Results are presented for the test cases outlined in the following section. The tables and figures of this chapter are shown in Appendices A and B, respectively.

4.1 Overview of Test Cases and Grid Details

Computational results are presented for the following test cases:

1. NACA 0012 airfoil at $M_\infty = 0.16$, $\alpha = 0°$, $Re = 2.88 \times 10^6$, transition at 0.43 chords on both surfaces.

2. NACA 0012 airfoil at $M_\infty = 0.16$, $\alpha_{corr} = 6°$, $Re = 2.88 \times 10^6$, transition at 0.05 and 0.8 chords on the upper and lower surfaces, respectively.

3. NACA 0012 airfoil at $M_{\infty_{corr}} = 0.7$, $\alpha_{corr} = 3°$, $Re = 9.0 \times 10^6$, transition at 0.05 chords on both surfaces.

4. RAE 2822 airfoil at $M_{\infty_{corr}} = 0.729$, $\alpha_{corr} = 2.31°$, $Re = 6.5 \times 10^6$, transition at 0.03 chords on both surfaces.

5. RAE 2822 airfoil at $M_{\infty_{corr}} = 0.754$, $\alpha_{corr} = 2.57°$, $Re = 6.2 \times 10^6$, transition at 0.03 chords on both surfaces.

6. NACA 0012 airfoil at $M_\infty = 0.01, 0.05, 0.1, 0.2, 0.3, 0.4$, $\alpha = 2.0°$, $Re = 2.88 \times 10^6$, transition at 0.05 and 0.25 on the upper and lower surfaces, respectively.

Several grids are used to evaluate the test cases. The grids are summarized in Table A.1 and all have a 'C' topology. In Table A.1, 'JDIM' represents the number of points in the streamwise direction, 'KDIM' represents the number of points in the normal direction, 'Body Points' represents the number of points on the body, 'Wake Points' represents the number of points in the wake, and 'Off-Wall Spacing' is the normal spacing to the first grid line off of the surface in chords. The distance to the outer boundary is 12 chords for all grids. The leading and trailing edge clustering for grid A is 0.0001 chords. Grid B was produced by removing every second node from grid A. Grid D was obtained by removing every second node from a larger grid having 497×97 nodes with an off-wall spacing of 1×10^{-6} and clustering the same as for grid A7A. Grid P is discussed in greater detail in section 4.4. The grids were generated using a hyperbolic grid generator; two samples are shown in Fig. B.1.

Reference solutions which are considered grid independent were obtained from a grid having approximately 500,000 nodes and are shown in Table A.2 for the first five test cases. The grid contained 1057 nodes in the streamwise direction, 497 nodes in the normal direction, 801 points on the body, 129 points in the wake, and an off-wall spacing of 2.3×10^{-7} chords. The reference solutions are used to estimate numerical errors (given as % error) in lift, drag, and the individual drag components, pressure drag and friction drag on the coarser grids. The values given in Table A.2 were obtained with matrix dissipation.

4.2 Parameter Studies

Two free parameters were introduced in section 3.3 for the CUSP scheme, namely κ_4 and ε. The parameter κ_4 scales the third-order dissipation, while ε is used to prevent random triggering of the limiter. Various values of these parameters were evaluated for the first five test cases and similar results were obtained. In the following sections, the parameter studies are presented for cases 1 and 3 to justify the selection of optimal values of κ_4 and ε used later to evaluate accuracy.

4.2.1 Test Case 1 - Subsonic Flow

This case was used to examine the effect of κ_4 on the solution without the interference from a limiter. The results are presented for grid D. Limiters are not required since the subsonic flow field does not contain any discontinuities. Recall that the original

CUSP scheme is obtained when $\kappa_4 = 1.0$. Reducing the value of κ_4 reduces the amount of third-order dissipation, and therefore, has the potential to increase the accuracy of the solution. However, lower dissipation may have a negative impact on the convergence rate. A number of numerical experiments were carried out to determine the optimal value of κ_4.

Table A.3 summarizes the results as κ_4 is reduced from 1.0 to 0.1 with the limiter turned off. These results indicate that as κ_4 is reduced, the error in drag and individual drag components becomes larger. Hence, reducing the dissipation did not improve the accuracy of the solution. Frew and Zingg [10] note that errors in global quantities, such as drag given in Table A.3, must be assessed with care since cancellations are possible on several levels. First, the error from numerical dissipation can cause an error of opposite sign to that from the truncation error of the centered difference scheme. Second, the local error can vary in sign in different portions of the flow field. Finally, the pressure and friction drag errors can be of opposite sign. In this case, it appears that even with $\kappa_4 = 1.0$ the truncation error already dominates the drag calculation. By reducing the dissipation further the truncation error becomes larger relative to the dissipation, and consequently, less accurate results are obtained. The convergence rate was not significantly affected down to $\kappa_4 = 0.25$, however, for $\kappa_4 = 0.1$ the solution diverged.

Comparison of the CUSP scheme with $\kappa_4 = 1.0$ to matrix dissipation with $V_n = V_l = 0$ reveals that the results are very similar, as shown in Table A.3. Note that with $V_n = V_l = 0$ the dissipation is minimum for the matrix scheme, although further numerical experiments may be required to ensure that current value of κ_4 is optimal for matrix dissipation. Hence, it appears that the CUSP scheme can provide less dissipation (with sufficiently small κ_4) than the matrix scheme. This could be useful if higher-order schemes are implemented which have a lower truncation error than the present second-order solver.

With no limiting and values of κ_4 below 0.5, a minor oscillation develops in the C_p plot around the transition points, as shown in Fig. B.2 where the symbol 'k(4)' denotes κ_4. In order to eliminate the oscillations, limiting was introduced which added first-order dissipation to the solution. Both, the V and Z limiters, defined in section 3.3.3, eliminated the oscillation, as shown in Fig. B.3 where the symbol 'eps' represents the parameter ε for the corresponding limiter.

Activating the limiter has an effect on the accuracy of the solution which is shown in Table A.4 for two values of ε per limiter and $\kappa_4 = 0.25$. Results presented in Table A.4 must be interpreted carefully. With the limiter activated, first-order dissipation is intro-

duced to the flow, which in this case favorably cancels the truncation error resulting in lower drag errors. Note that with the limiter and low κ_4 the results are not significantly different from the results obtained with no limiting and $\kappa_4 = 1.0$. Further, activating the limiter adds considerable computational expense, as discussed in section 4.5. Thus for subsonic flows, best results are obtained without limiting and with $\kappa_4 = 1.0$.

4.2.2 Test Case 3 - Transonic Flow

Transonic flows require limiters to activate in the region of flow discontinuities, such as shocks, to ensure good convergence rates and to preserve the monotonicity of the solution. For the V and Z limiters introduced in Eqs. 3.40 and 3.41 a value of ε must be selected such that limit cycles are avoided yet reasonably oscillation-free shocks are obtained. A parameter search was performed to find values of ε and κ_4 for which accuracy, shock capturing, and convergence are optimum. First, with κ_4 held constant at 1.0, a value for ε was selected. Next, the value of κ_4 was reduced to see if the solution can be further improved.

Various values of ε were evaluated for the V and Z limiters. The accuracy results for grid D are shown in Table A.5. Note that for both limiters, more first-order dissipation is introduced as ε is reduced. Smallest errors in the aerodynamic coefficients were obtained with relatively large values of ε, specifically 20.0 with the V limiter, and 0.01 for the Z limiter. With these values, the limiters introduce less first-order dissipation, and therefore, greater accuracy is achieved. Values of ε below 1×10^{-4} for the Z limiter and 5.0 for the V limiter yield large errors in drag when compared to the matrix scheme. Pressure drag is more sensitive to ε than skin friction drag. Note that for this case, matrix dissipation predicts the skin friction drag coefficient more accurately than the CUSP scheme.

Shock capturing for the same range of ε values as given in Table A.5 was examined for both limiters and the results are shown in Figs. B.4 and B.5. Shocks with two interior points are obtained for all values of ε. For the V limiter, values of ε should not exceed 10.0, while for the Z limiter, the values should be kept below 0.01 in order to obtain oscillation-free shocks. Note that the CUSP scheme with the limiters resolves shocks better than the matrix scheme with the pressure switch.

Lastly, the effect of ε on the convergence rate of the solver was evaluated. Fig. B.6 shows the convergence rate for both limiters. For the V limiter, best convergence rates were

obtained for values of ε equal to 3.0 and 5.0. For the Z limiter, the convergence rate stalled for values of ε below 1×10^{-3}. Generally, if the convergence rate stalls as the residual passes through the first two orders of magnitude, the limiter is trapped in a limit cycle. For the cases shown in Fig. B.6, the stall in the convergence rate is due to the Baldwin-Lomax turbulence model, and in order to converge the solution further the turbulence model must be frozen.

Hence, in terms of accuracy, shock capturing, and convergence rate, the V Limiter performs well with values of ε between 3.0 and 10.0, while the Z limiter performs well with values of ε between 1×10^{-2} and 1×10^{-4}. Similar results were observed for the other transonic test cases. The optimal values of ε were chosen to be 5.0 for the V limiter, and 1×10^{-3} for the Z limiter.

Having selected ε, the parameter κ_4 was reduced from 1.0 in order to test if the accuracy of the solution can be improved. Unfortunately, this was not the case. For values of κ_4 below 0.5 the solution diverged, and for κ_4 greater than 0.5 the improvements in accuracy were insignificant. This may be due to the fact that for transonic cases first-order dissipation and the shock-induced separation region heavily influence the accuracy of the solution. Therefore, the use of κ_4 other than 1.0 is not recommended for transonic calculations.

4.3 Accuracy Studies

Optimal values for ε and κ_4 were selected in section 4.2 for both subsonic and transonic flow. With those parameters, the CUSP scheme is evaluated for the test cases $1 - 5$ with a focus on accuracy, shock capturing, and convergence rate. The results are compared to the matrix and scalar dissipation models.

4.3.1 Subsonic Cases

The flow field for cases 1 and 2 is subsonic and does not contain any discontinuities. Therefore, it is possible to study the performance of third-order dissipation alone, without the influence from first-order dissipation. Consequently, the user selected parameters for scalar and matrix dissipation were set to $\kappa_2 = 0$ and $\kappa_4 = 0.64$. For matrix dissipation, values of $V_n = V_l = 0$ were used. For CUSP dissipation, limiters were not activated ($R(u, v) = 1$), and $\kappa_4 = 1$.

Table A.6 shows the numerical errors in drag obtained for case 1. The entries give the percent difference in the drag coefficient, C_d, the pressure drag component, C_{d_p}, and the friction drag component, C_{d_f}, from the grid-independent result given in Table A.2. First, it should be noted that both matrix and CUSP dissipation lead to a marked reduction in error when compared to scalar dissipation. This is especially evident on the coarser grid D. Second, the values obtained using CUSP dissipation are very similar to those obtained with matrix dissipation. The results suggest that to obtain aerodynamic coefficients to within 1% of the converged values, a grid with $24,000$ nodes (grid B) is required.

The numerical errors shown in Table A.6 consist of the second-order truncation error of the centered difference scheme and the third-order numerical dissipation. The local flux balance of the convective flux, the viscous flux, and the numerical dissipation is used to distinguish between these two contributions. In boundary layers, the streamwise momentum equation is typically most revealing.

Fig. B.7 shows the x-momentum flux balance for case 1 computed on grid B using the scalar, matrix, and CUSP numerical dissipation models respectively. The station shown is at $x/c = 0.24$ where the flow is laminar and the boundary layer thickness is roughly 0.002 chords. There are approximately 45 points across the boundary layer. Ideally, the viscous flux should balance the convective flux with only a minimal contribution from the numerical dissipation. This is best shown in Fig. B.7b for matrix dissipation. The performance of the CUSP scheme, Fig. B.7c, is similar to matrix dissipation, with some differences just outside of the boundary layer. These differences are attributed to the higher effective coefficient for the third-order dissipation of the CUSP scheme when compared to the matrix scheme, as discussed in section 3.3.3. With the scalar dissipation model, the numerical dissipation exceeds the viscous flux through much of the boundary layer. Note that the influence of the scalar dissipation model is particularly large for this case as a result of the low Mach number.

Fig. B.8 shows the x-momentum flux balance at station $x/c = 0.6$ on grid B for case 1. Here, the flow is turbulent and the boundary layer thickness is 0.008 chords. There are roughly 55 points across the boundary layer. Both CUSP and matrix dissipation obtain excellent flux balances. Scalar dissipation introduces too much dissipation in the boundary layer, and consequently, poor flux balances are obtained.

The boundary layer velocity profiles are shown in Fig. B.9. The matrix and CUSP schemes produce very similar profiles, in both the laminar and turbulent regions of the flow.

These results are not surprising, since both schemes obtained good flux balances. For the scalar model at station $x/c = 0.24$, note the aphysical overshoot in the outer portion of the boundary layer, which was also observed by Frew and Zingg [10]. The turbulent boundary layer, Fig. B.9b, is relatively thick and extends into a coarse region of the grid. At the turbulent station, scalar dissipation underpredicts the velocity, while CUSP and matrix dissipation both overpredict the velocity. Note the overshoot with scalar dissipation at the exit from the boundary layer. The solution labeled as 'reference' was obtained on the finest grid ($500,000$ nodes).

Accurate prediction of skin friction drag depends on the boundary layer velocity profile. The skin friction coefficient, normalized by the freestream dynamic pressure, is shown in Fig. B.10 for case 1. On the intermediate grid B, Fig. B.10a, scalar dissipation produces a skin friction coefficient which is too high in the laminar portion of the flow and too low in the turbulent portion of the flow. Both matrix and CUSP schemes obtain results which are much closer to the reference solution. The CUSP scheme captures the transition from the laminar to turbulent flow slightly better. In Fig. B.10b, the skin friction coefficient is shown for grid D, as obtained by the matrix and CUSP schemes. Again, it is difficult to distinguish between the two schemes. Both schemes slightly underpredict the skin friction coefficient in the laminar and turbulent regions.

For case 2, the errors in the aerodynamic coefficients are higher, as shown in Table A.7. However, matrix and CUSP dissipation predict the value of skin friction drag significantly better than scalar dissipation on the coarser grid D. Fig. B.11 shows the skin friction coefficient, and it should be noted that on grid D matrix dissipation performs slightly better than CUSP. For the CUSP scheme, the skin friction coefficient on the upper surface is lower than the reference and matrix values, while on the lower surface it is higher than the reference value. Therefore, some error cancellation may have affected the global skin friction drag result. In Fig. B.11a, matrix and CUSP predict skin friction coefficient equally well on the intermediate grid B.

As Table A.7 indicates, the errors in lift coefficient are small for all schemes, and the greatest error for this case is in the pressure drag. At the angle of attack of 6°, the influence of pressure stretches outside of the boundary layer where the grid is relatively coarse, and hence, accurate prediction of the pressure drag may be difficult. Overall for case 2, the results obtained by the CUSP scheme are similar to the results obtained by matrix dissipation. Scalar dissipation is unable to predict skin friction drag accurately on

the coarser grids.

The convergence histories for cases 1 and 2 are shown in Figs. B.12 and B.13. The different numerical dissipation models have little effect on the convergence rate. The convergence histories obtained using CUSP and matrix dissipation are particularly similar.

4.3.2 Transonic Cases

Tables A.8, A.9, and A.10 show the estimates of the numerical errors in lift, drag, and individual drag components for the transonic cases 3, 4, and 5 respectively. The label 'CUSP V' denotes CUSP dissipation with the V limiter given by Eq. 3.40, while 'CUSP Z' denotes CUSP dissipation with the Z limiter given by Eq. 3.41. The results for matrix dissipation were obtained with the following parameter settings: for case 3, $V_n = 0.25$ and $V_l = 0.025$; for case 4, $V_n = 0.25$ and $V_l = 0.1$; and for case 5, $V_n = V_l = 0.3$. The coefficient $\kappa_2 = 2.0$ and $\kappa_4 = 0.64$ for scalar and matrix dissipation for all transonic cases. For the CUSP scheme, $\kappa_4 = 1.0$ and the following limiter constants were used: $\varepsilon = 5$ for the V limiter, and $\varepsilon = 1 \times 10^{-3}$ for the Z limiter.

The absolute errors in lift coefficients do not exceed 2% for all three schemes even on the coarser grid D. For the drag coefficients, CUSP dissipation appears to be most accurate, but matrix dissipation is generally within 1% of CUSP's results. Matrix dissipation is able to predict friction drag slightly more accurately than the CUSP scheme. For the pressure drag, results are generally within 1% of each other for the CUSP and matrix schemes. Hence, some error cancellation may have contributed to the fact that the CUSP scheme obtained better global drag coefficients. The two limiters produce similar results, with the Z limiter perhaps slightly more accurate (for example, see case 3 for grid D). Scalar dissipation is not competitive with the more sophisticated dissipation models, especially in skin friction results on the coarser grids.

Fig. B.14 shows the flux balance at 98% chord where the flow begins to separate for case 3 on grid C. The skin friction drag from Table A.8 indicates that all three dissipation schemes should obtain approximately the same flux balances. Close to the airfoil this is indeed the case; the contribution of the dissipation is minimal for all three schemes. The best flux balance is obtained by matrix dissipation due to the low third-order dissipation coefficient. The scalar and CUSP schemes produce equivalent results.

The friction drag coefficient for case 3 is shown in Fig. B.15 for grids A and C

respectively, and Fig. B.16 for grid D. In Fig. B.15, matrix and CUSP dissipation obtained identical results, especially on the fine grid A. Both schemes predict the shock-induced separation region at approximately 35% chord on grid A and grid C. Results from scalar dissipation show significant deviation from matrix and CUSP results on grid C, particularly downstream of the shock. On the coarser grid D, the CUSP scheme captures the shock-induced separation region significantly better than the matrix and scalar models, as shown in Fig. B.16. This can be attributed to the more sophisticated limiters used by the CUSP scheme, instead of the pressure switch used by matrix dissipation. However, in the region downstream of the shock on the upper surface, matrix dissipation is closer than CUSP to the reference solution. The V and Z limiters produced identical solutions.

Figs. B.17 and B.18 show the skin friction coefficient for cases 4 and 5. Observations which can be made from these figures are similar to the observations made for case 3. The shock-induced separation region is best predicted by the CUSP scheme, with both limiters performing equally well. For case 4, especially on the lower surface, the matrix scheme performs slightly better than CUSP. For case 5, the CUSP scheme underpredicts the skin friction coefficient while matrix dissipation overpredicts the skin friction on the lower surface. In this region, CUSP is closer to the reference solution. Both the matrix, and CUSP schemes are successful at predicting the small separation region at the trailing edge. Scalar dissipation is not competitive with the more sophisticated models on grid D.

Pressure coefficient distributions for cases 3, 4, and 5 are plotted in Figs. B.19, B.20, and B.21 respectively. The CUSP scheme consistently produces sharper shocks than the matrix dissipation scheme, primarily due to the more sophisticated limiters used. All shocks obtained by the CUSP scheme are oscillation-free and have two interior points. With the matrix scheme, four-interior-point shocks are obtained with slight oscillations at the entrance and exit nodes. Scalar dissipation smears the shocks over 5 nodes. Swanson *et al.* [17] observed that for transonic viscous flow the HCUSP scheme captured shocks which were too far upstream. Clearly, the present results with ECUSP do not have the same difficulty, and the captured shock locations agree with both the scalar and matrix models.

The convergence histories for cases 3, 4, and 5 are shown in Figs. B.22, B.23, and B.24. The convergence of matrix dissipation is dependent on sufficiently high values of V_n and V_l. For the three cases, these values increased from 0.25 and 0.025 to 0.3 and 0.3 respectively. The parameters for the CUSP schemes did not require any adjustment, and consequently, the scheme could be considered more robust than the matrix scheme. How-

ever, as long as V_n and V_l do not exceed 0.3, they do not have a significant impact on drag for the transonic cases. The performance of the V and Z limiters is generally comparable. The stall in the convergence rates, which can be observed in Figs. B.22, B.23, and B.24, is due to the use of the Baldwin-Lomax turbulence model. To converge the solutions further the turbulence model must be frozen. Unfortunately, this is not a practical solution, and possibly using a different turbulence model and/or different grids may eliminate the problem.

4.4 Local Preconditioning Results

The performance of the CUSP scheme in conjunction with the preconditioned algorithm is evaluated for case 6 and the results are compared with the preconditioned scalar scheme, and with the original scalar, matrix, and CUSP schemes. For the preconditioned algorithm the parameters ϕ and χ were set to 1.0 and 0 respectively. For scalar and matrix dissipation, the following constants were used: $\kappa_2 = 0$ and $\kappa_4 = 0.64$. For matrix dissipation, values of $V_n = V_l = 0$ were used. For CUSP dissipation, the limiters were turned off, and $\kappa_4 = 1.0$.

Stability problems were encountered when the preconditioned CUSP scheme was evaluated on grid D. It was found that there was insufficient dissipation at the trailing edge of the airfoil, just as the grid lines enter the wake. The presence of high aspect ratio cells stretched in the normal direction with respect to the flow appeared to cause the solver to diverge. The problem was fixed with a new grid labeled P, which is very similar to grid D except it has 15 additional nodes in the wake, and less aggressive trailing edge clustering of 0.001 instead of 0.0002. The grid details are given in Table A.1. The stability problem suggests that the robustness of the preconditioned CUSP scheme should be further examined.

Fig. B.25 shows the variation of the computed drag and lift with the freestream Mach number for the original three numerical dissipation models. Also shown is the preconditioned result with scalar and CUSP dissipation. In Fig. B.25a, the preconditioned scalar and CUSP schemes correctly illustrate the lack of dependence of drag on the Mach number for the given Mach number range. Further, the drag obtained with the preconditioned CUSP scheme is lower than the drag obtained with the preconditioned scalar dissipation. The grid independent drag coefficient for this case is about 0.0084. The preconditioned

CUSP dissipation is within 1% of this result, while for the preconditioned scalar dissipation the error is 5%. Also, Fig. B.25a clearly shows that even the results obtained by the original matrix and CUSP dissipation without preconditioning are superior to the preconditioned scalar results down to a Mach number of 0.05. However, both matrix and CUSP dissipation without preconditioning show dependence on the Mach number for Mach numbers less than 0.15. This dependence is removed with the preconditioned CUSP scheme.

In Fig. B.25b, the variation of the lift coefficient with the Mach number is shown. For low Mach numbers, the original CUSP scheme without preconditioning predicts lift poorly. Fortunately, the problem is eliminated in the preconditioned algorithm, and this issue is discussed later. Note that the slope of the lift curve changes for matrix dissipation as well for Mach numbers below 0.1. Therefore, local preconditioning is necessary to improve the accuracy of lift results for low Mach numbers.

Figs. B.26a and B.26b show the convergence of drag for the scalar and CUSP schemes with and without local preconditioning for the freestream Mach number of 0.05. For the preconditioned algorithm, drag converges within 500 iterations, while without preconditioning, 2000 iterations are required to obtain a converged value. In Figs. B.27a and B.27b, the drag convergence is shown for a higher Mach number of 0.3. The gains of local preconditioning are significantly diminished. The drag values converge within 500 iterations, and for the CUSP scheme, the accuracy is not affected. For scalar dissipation, the preconditioned spectral radius produces more accurate results as discussed in greater detail by Unrau and Zingg [5].

Fig. B.28 shows the convergence of lift for the freestream Mach number of 0.05. The preconditioned scalar and CUSP values are identical, and convergence is obtained within 500 iterations. For the original algorithm, both the CUSP scheme and scalar scheme are not fully converged at $2,500$ iterations. The CUSP result is also significantly inaccurate. To examine the source of this problem, the C_p plot is shown in Fig. B.28b. The original CUSP scheme predicts C_p values which are too low on the upper surface and too high on the lower surface when compared to the preconditioned results. Also, oscillations were found upon closer examination of the trailing edge region.

Figs. B.29 and B.30 show the convergence history for the scalar and CUSP schemes with and without local preconditioning. Clearly, the convergence is significantly accelerated in the preconditioned algorithm for Mach numbers up to 0.2. The convergence rates are similar for both schemes.

4.5 Computational Efficiency

Table A.11 summarizes the computational efficiency of the three numerical dissipation schemes, normalized by the results for the nonlinear scalar model. With each scheme, a timed run was performed for 1000 iterations. For the CUSP scheme, the computational efficiency was evaluated for subsonic and transonic flows separately, to take advantage of some simplifications for subsonic flow.

With the matrix model, the extra cost is primarily associated with the formation of the matrix-vector product $|A|Q$. The results obtained for matrix dissipation are different from the results obtained by Frew and Zingg [10] who found that matrix dissipation is only 30% more expensive than scalar dissipation. This is due to the fact that Frew and Zingg [10] treated the wake cut implicitly which reduced the overall efficiency of the solver.

For CUSP dissipation, the extra cost is primarily associated with the more complicated limiter. The limiter value has to be computed for each state variable at each node for each direction (i.e., eight evaluations of the limiter function) compared to just two evaluations per node of the pressure switch function. Further, on the left-hand-side of the implicit algorithm, the pentadiagonal matrix associated with the first two eigenvalues of the flux Jacobian can be inverted simultaneously for scalar and matrix dissipation. Since the limiter applies a different value to each conservation equation, an extra loop is required to evaluate the left-hand-side.

For subsonic flow with Mach numbers less than 0.5, the formation of the flux vector difference is not required in the CUSP scheme. Also, it is not necessary to use the limiter, which speeds up the code significantly, as shown in Table A.11. Further improvements are possible in the programming implementation of the CUSP scheme to bring its efficiency closer to the scalar scheme for subsonic flow.

For transonic flow, the Z limiter is more efficient than the V limiter. The V limiter contains a 'max' function, and also, requires evaluation of the grid spacing in the physical domain. Therefore, the Z limiter is recommended for transonic computations.

Generally, the efficiency of the centered-difference algorithm coupled with scalar dissipation is approximately twice the efficiency of a TVD scheme. The results obtained indicate that the CUSP scheme with the sophisticated limiter, or the matrix scheme with the pressure switch are then approximately 1.5 as efficient as a TVD scheme, which is illustrated in Fig. 4.1. Swanson *et al.* [17] found CUSP dissipation 40% more expensive

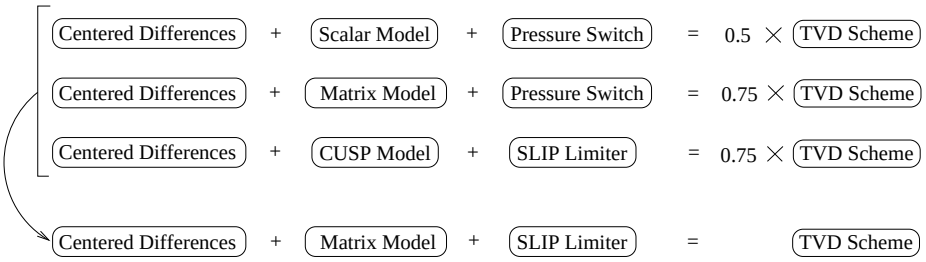

Figure 4.1: Numerical dissipation and TVD schemes.

than the scalar scheme, while matrix dissipation was only 15% above the scalar scheme. The results obtained for the CUSP scheme agree with Swanson *et al.* [17], but there is significant disagreement for matrix dissipation with our solver.

Chapter 5

Conclusions and Recommendations

The implementation of the ECUSP [12, 13] scheme in the approximately-factored algorithm SC1 [19] has been presented and applied to several turbulent aerodynamic flows. The CUSP scheme was implemented in conjunction with two SLIP limiters [12], namely the V and Z limiters. Further, the CUSP scheme was modified to work in conjunction with local preconditioning [5] for flows at low Mach number. The results obtained were compared with the scalar [2] and matrix [7] dissipation schemes. A detailed evaluation of the CUSP scheme was performed with emphasis on the following criteria: 1) accuracy, 2) robustness, and 3) computational cost. The conclusions with respect to these three criteria are summarized below:

1. Algorithm accuracy:

   - The CUSP scheme is superior to the scalar scheme and comparable in accuracy to matrix dissipation.
   - The CUSP scheme is not a total-variation-diminishing scheme. Although it performed well for the selected aerodynamic computations, it is not suited for general-purpose applications.
   - Oscillation-free, two-interior-point shocks are obtained with the CUSP scheme. Matrix dissipation with the pressure switch requires four nodes to resolve shocks, while the scalar scheme smears shocks over five nodes.
   - Both V and Z limiters produced good results in terms of accuracy.

- For low Mach number flow, the preconditioned CUSP scheme is more accurate than the preconditioned scalar scheme, and the original matrix and CUSP schemes.

2. Algorithm robustness:

   - The CUSP scheme avoids the need to find suitable values of V_n and V_l as required by the matrix scheme.
   - In conjunction with local preconditioning, slight grid modifications were required to obtain convergence to steady-state with the CUSP scheme.
   - For Mach numbers below 0.2, the convergence of the aerodynamic coefficients was significantly accelerated with the preconditioned algorithm.
   - With the original algorithm, the CUSP scheme obtained good convergence in all cases studied.

3. Computational cost:

   - The matrix scheme is computationally more expensive than the CUSP scheme, since the CUSP scheme avoids the evaluation of matrix-vector products.
   - The cost of the SLIP limiter implemented in conjunction with the CUSP scheme is on average 20% greater than the pressure switch implemented with the scalar and matrix schemes.
   - The Z limiter was found to be more computationally efficient than the V limiter, and therefore the Z limiter is recommended for transonic calculations.

Overall, the results show the CUSP scheme to be very effective in providing good shock capturing, low numerical dissipation in boundary layers, and low numerical errors in drag. However, the results indicate that improvements in computational efficiency and performance are still desired. The computational cost could be reduced by implementing the pressure switch in conjunction with the CUSP scheme. Further research into modifying the CUSP scheme to satisfy the TVD criteria would allow the scheme to be applied to a more general class of problems. Additional recommendations for future research are to improve to the robustness of the preconditioned CUSP scheme, and to evaluate the SLIP limiter in conjunction with matrix dissipation.

References

[1] Pulliam, T. H., "Efficient Solution Methods For The Navier-Stokes Equations." Lecture Notes For The Von Karman Institute For Fluid Dynamics Lecture Series: *Numerical Techniques For Viscous Flow Computation In Turbomachinery Bladings*, Jan. 1986.

[2] Jameson, A., Schmidt, W. and Turkel, E., "Numerical Solutions of the Euler Equations by Finite Volume Methods Using Runge-Kutta Time-Stepping." AIAA Paper 81-1259, June 1981.

[3] Allmaras, S. R., "Contamination of Laminar Boundary Layers by Artificial Dissipation in Navier-Stokes Solutions," in *Numerical Methods for Fluid Dynamics* (M. J. Baines and K. W. Morton, eds.), Clarendon Press, Oxford, 1993.

[4] Reddy, S. and Papadakis, M., "Artificial Viscosity Models for the Navier-Stokes Equations and Their Effect in Drag Prediction." AIAA Paper 93-0193, Jan. 1993.

[5] Unrau, D. and Zingg, D. W., "Viscous Airfoil Computations Using Local Preconditioning." AIAA Paper 97-2027, June 1997.

[6] Weiss, J. M. and Smith, W. A., "Preconditioning Applied to Variable and Constant Density Flows," *AIAA Journal*, vol. 33, no. 11, pp. 2050–2057, 1995.

[7] Swanson, R. C. and Turkel, E., "On Central-Difference And Upwind Schemes." NASA CR-182061, 1990.

[8] Turkel, E., "Improving the Accuracy of Central Difference Schemes." NASA CR-181712, 1988.

[9] Turkel, E. and Vatsa, V. N., "Effect of Artificial Viscosity on Three-Dimensional Flow Solutions," *AIAA Journal*, vol. 32, pp. 39–45, 1994.

[10] Frew, K. and Zingg, D. W., "On Artificial Dissipation Models for Viscous Airfoil Computations." AIAA Paper 96-1970, June 1996.

[11] Venkatakrishnan, V., "Convergence to Steady State Solutions of the Euler Equations on Unstructured Grids with Limiters," *Journal of Computational Physics*, vol. 118, pp. 120–130, 1995.

[12] Jameson, A., "Analysis and Design of Numerical Schemes for Gas Dynamics I: Artificial Diffusion, Upwind Biasing, Limiters and their Effect on Accuracy and Multigrid Convergence," *Inter. J. Comput. Fluid Dynamics*, vol. 4, pp. 171–218, 1995.

[13] Jameson, A., "Analysis and Design of Numerical Schemes for Gas Dynamics II: Artificial Diffusion, and Discrete Shock Structure," *Inter. J. Comput. Fluid Dynamics*, vol. 5, pp. 1–38, 1995.

[14] Liou, M-S. and Steffen Jr., C. J., "A New Flux Splitting Scheme," *Journal of Computational Physics*, vol. 107, pp. 23–39, 1993.

[15] Edwards, J. R. and Liou, M-S., "Low-Diffusion Flux-Splitting Methods for Flows at All Speeds." AIAA Paper 97-1862, June 1997.

[16] Tatsumi, S., Martinelli, L. and Jameson, A., "A New High Resolution Scheme for Compressible Viscous Flow with Shocks." AIAA Paper 95-0466, Jan. 1995.

[17] Swanson, R. C., Radespiel, R. and Turkel, E., "Comparison of Several Dissipation Algorithms for Central Difference Schemes." AIAA Paper 97-1945, June 1997.

[18] Tweedt, D. L., Chima, R. V. and Turkel, E., "Preconditioning for Numerical Simulation of Low Mach Number Three-Dimensional Viscous Turbomachinery Flows." AIAA Paper 97-1828, 1997.

[19] De Rango, S. and Zingg, D. W., *SC1 User's Guide*. University of Toronto Institute for Aerospace Studies, 1997.

Appendix A

Tables

Grid	JDIM	KDIM	Body Points	Wake Points	Off-Wall Spacing
A	497	193	401	49	1×10^{-7}
B	249	97	201	25	2×10^{-7}
C	321	75	257	33	8×10^{-7}
D	249	49	201	25	2×10^{-6}
P	279	49	201	40	2×10^{-6}

Table A.1: Summary of grids.

Test Case	C_l	C_d	C_{d_p}	C_{d_f}
Case 1	-	0.00579	0.00081	0.00498
Case 2	0.6658	0.00782	0.00254	0.00528
Case 3	0.5116	0.01361	0.00863	0.00498
Case 4	0.7966	0.01345	0.00823	0.00522
Case 5	0.8484	0.03034	0.02533	0.00505

Table A.2: Grid independent results.

Dissipation	κ_4	$\%C_d$	$\%C_{d_p}$	$\%C_{d_f}$
CUSP	1.0	-2.7	-0.1	-3.1
CUSP	0.5	-3.2	-2.7	-3.2
CUSP	0.25	-3.7	-3.0	-3.9
CUSP	0.1	DNC	DNC	DNC
Matrix	-	-2.5	-0.9	-2.7

Table A.3: Case 1 parameter study for κ_4 without limiter.

Dissipation	κ_4	Limiter	ε	$\%C_d$	$\%C_p$	$\%C_f$
CUSP	0.25	Z	1×10^{-3}	-3.5	-3.5	-3.5
CUSP	0.25	Z	1×10^{-4}	-2.9	-2.3	-3.0
CUSP	0.25	V	1.0	-1.1	7.8	-2.6
CUSP	0.25	V	5.0	-2.4	2.4	-3.1
Matrix	-	-	-	-2.5	-0.9	-2.7

Table A.4: Case 1 with limiter and low κ_4.

Dissipation	Limiter	ε	C_l	C_d	C_{d_p}	C_{d_f}
CUSP	Z	0.01	-2.3	-1.0	1.3	-4.9
CUSP	Z	0.001	-2.0	0.1	3.0	-4.8
CUSP	Z	1×10^{-4}	-1.9	1.5	4.9	-4.6
CUSP	Z	1×10^{-5}	-1.9	2.6	6.7	-4.4
CUSP	V	1.0	-1.9	2.2	6.1	-4.5
CUSP	V	5.0	-2.0	0.5	3.6	-4.8
CUSP	V	10.0	-2.0	0.1	2.9	-4.7
CUSP	V	20.0	-2.3	-0.7	1.6	-4.7
Matrix	-	-	-1.7	2.8	5.4	-1.6

Table A.5: Sensitivity of solution to ε for Case 3 ($M_\infty = 0.7$, $\alpha = 3°$, $\kappa_4 = 1.0$).

Grid	Diss.	$\%C_d$	$\%C_{d_p}$	$\%C_{d_f}$
A	CUSP	< 0.05	0.1	< 0.05
	Matrix	-0.1	-0.5	< 0.05
	Scalar	0.8	0.7	0.9
B	CUSP	0.4	1.6	0.2
	Matrix	0.2	0.1	0.3
	Scalar	3.5	8.3	2.7
D	CUSP	-2.7	-0.1	-3.1
	Matrix	-2.5	-0.9	-2.7
	Scalar	41.9	28.6	44.1

Table A.6: Grid study for Case 1: NACA 0012 at $M_\infty = 0.16$ and $\alpha = 0°$.

Grid	Diss.	$\%C_l$	$\%C_d$	$\%C_{d_p}$	$\%C_{d_f}$
A	CUSP	-0.5	1.2	3.4	-0.1
	Matrix	-0.6	2.0	6.3	-0.1
	Scalar	-0.6	1.8	4.4	0.5
B	CUSP	< 0.05	4.8	15.8	-0.5
	Matrix	-0.2	6.2	19.9	-0.3
	Scalar	-0.2	7.4	19.8	1.4
D	CUSP	-2.2	14.4	55.0	-5.1
	Matrix	-1.5	14.6	51.3	-3.0
	Scalar	-1.8	47.9	61.6	41.4

Table A.7: Grid study for Case 2: NACA 0012 at $M_\infty = 0.16$ and $\alpha = 6°$.

Grid	Diss.	$\%C_l$	$\%C_d$	$\%C_{d_p}$	$\%C_{d_f}$
A	CUSP V	-1.4	-1.4	-1.7	-1.0
	CUSP Z	-1.4	-1.6	-2.0	-1.0
	Matrix	-1.1	-1.0	-1.3	-0.5
	Scalar	-1.0	-0.7	-1.0	-0.3
C	CUSP V	-1.3	0.2	1.4	-1.8
	CUSP Z	-1.3	-0.2	0.8	-1.9
	Matrix	-1.0	0.9	2.1	-1.1
	Scalar	-1.2	3.0	2.9	3.1
D	CUSP V	-2.0	0.5	3.6	-4.8
	CUSP Z	-2.0	0.1	3.0	-4.8
	Matrix	-1.7	2.8	5.4	-1.6
	Scalar	-2.7	12.3	8.4	19.0

Table A.8: Grid study for Case 3: NACA 0012 at $M_\infty = 0.7$ and $\alpha = 3°$.

Grid	Diss.	$\%C_l$	$\%C_d$	$\%C_{d_p}$	$\%C_{d_f}$
A	CUSP V	-0.7	< 0.05	0.2	-0.2
	CUSP Z	-0.8	-0.3	-0.3	-0.2
	Matrix	-0.4	-0.1	-0.1	-0.1
	Scalar	-0.3	0.4	0.7	-0.1
C	CUSP V	-0.5	2.7	5.1	-0.9
	CUSP Z	-0.6	2.3	4.4	-1.0
	Matrix	-0.6	2.9	4.9	-0.2
	Scalar	-0.7	4.4	6.3	1.4
D	CUSP V	-0.9	4.8	5.1	-2.8
	CUSP Z	-0.8	4.8	4.4	-2.8
	Matrix	-1.6	5.7	9.6	-0.4
	Scalar	-2.2	13.1	13.6	12.2

Table A.9: Grid study for Case 4: RAE 2822 at $M_\infty = 0.729$ and $\alpha = 2.31°$.

Grid	Diss.	$\%C_l$	$\%C_d$	$\%C_{d_p}$	$\%C_{d_f}$
A	CUSP V	-1.2	-2.1	-1.8	-1.1
	CUSP Z	-1.2	-1.7	-1.9	-1.1
	Matrix	-1.1	-1.9	-2.3	-1.0
	Scalar	-0.9	-1.4	-1.8	-0.3
C	CUSP V	-1.2	-0.2	-0.2	-1.0
	CUSP Z	-1.1	< 0.05	0.1	-1.1
	Matrix	-0.3	-0.8	-0.9	-0.4
	Scalar	-1.6	-0.3	-0.7	1.0
D	CUSP V	-2.4	-0.4	< 0.05	-3.0
	CUSP Z	-2.6	-0.5	-0.1	-3.1
	Matrix	-3.7	-3.0	-3.8	0.6
	Scalar	-2.7	1.9	0.4	8.7

Table A.10: Grid study for Case 5: RAE 2822 at $M_\infty = 0.754$ and $\alpha = 2.57°$.

Dissipation	Subsonic Flow	Transonic Flow
Scalar	1.0	1.0
Matrix	1.5	1.5
CUSP V	1.3	1.6
CUSP Z	1.3	1.4

Table A.11: Computational efficiency (error $\approx \pm 0.05$).

Appendix B

Figures

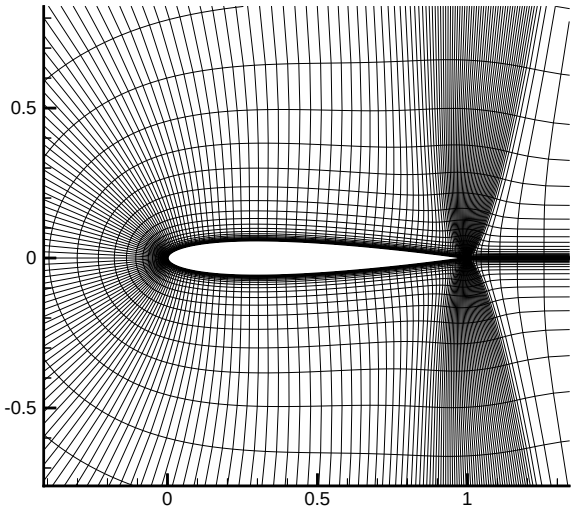

(a) Close-up of NACA 0012 airfoil.

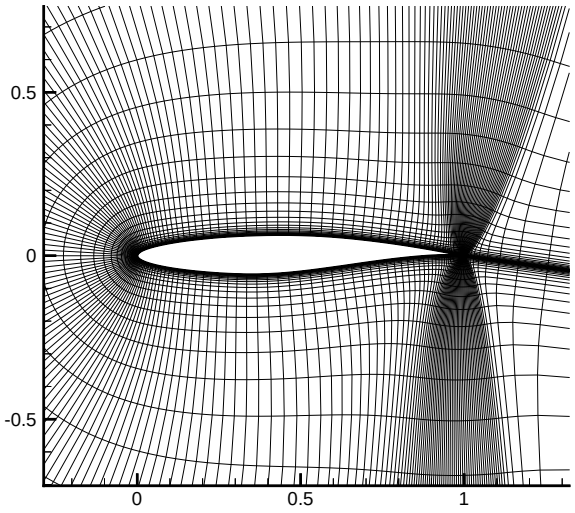

(b) Close-up of RAE 2822 airfoil.

Figure B.1: Example of 'C' mesh for grid D.

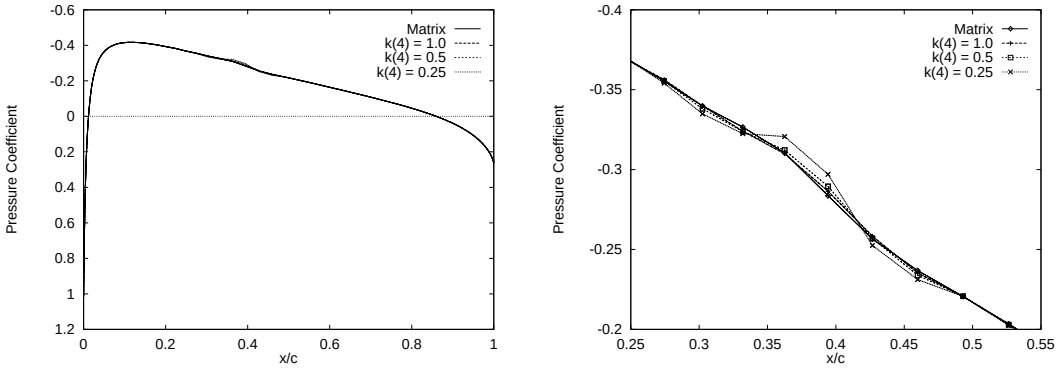

(a) C_p (b) Close-up of transition region.

Figure B.2: Effect of lowering κ_4 without limiters on C_p for Case 1.

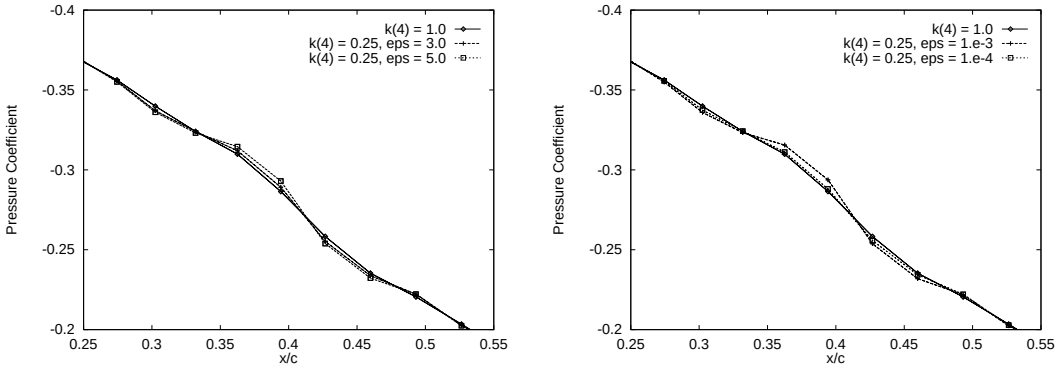

(a) Close-up of transition with V limiter. (b) Close-up of transition with Z limiter.

Figure B.3: Use of limiters with low κ_4 for Case 1.

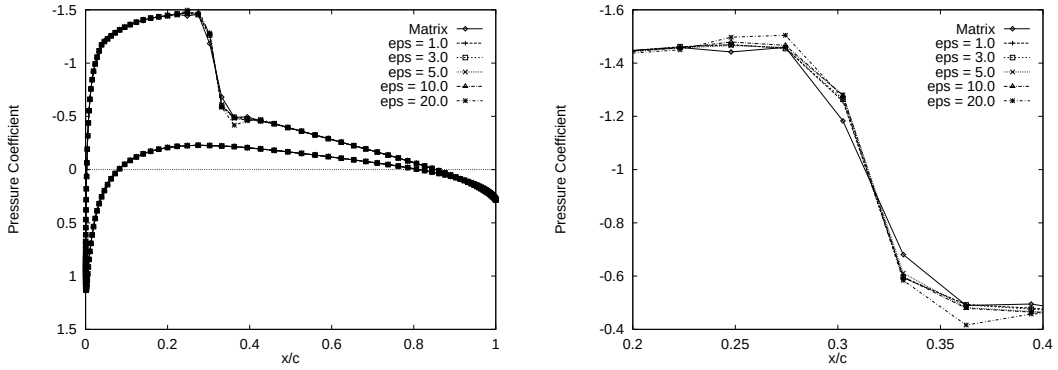

(a) C_p (b) Close-up of shock region.

Figure B.4: Shock capturing with V limiter for Case 3 ($M_\infty = 0.7$, $\alpha = 3°$, $\kappa_4 = 1.0$).

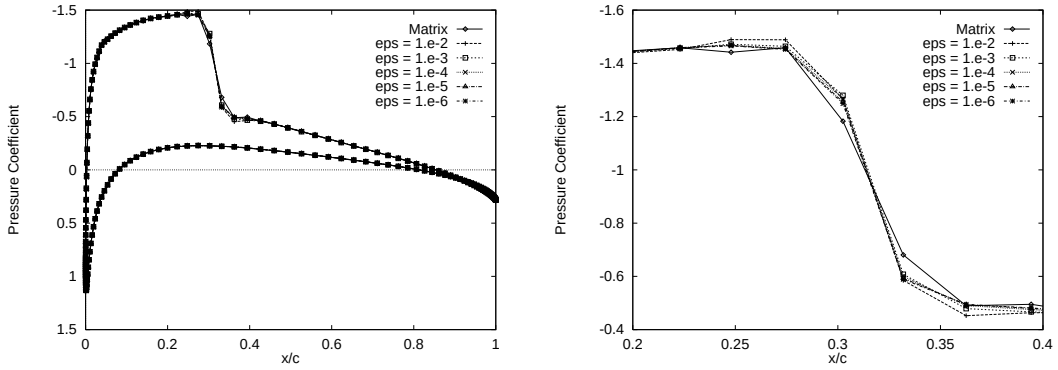

(a) C_p (b) Close-up of shock region.

Figure B.5: Shock capturing with Z limiter for Case 3 ($M_\infty = 0.7$, $\alpha = 3°$, $\kappa_4 = 1.0$).

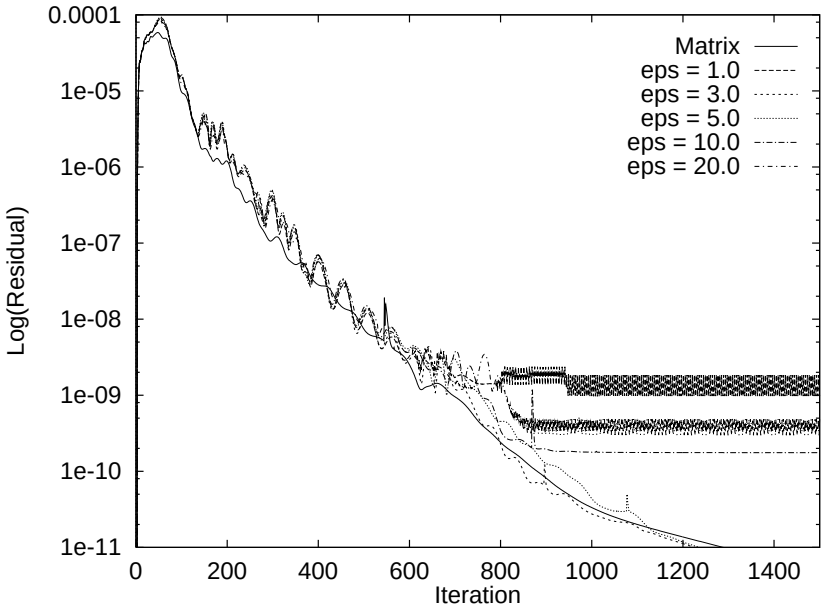

(a) Convergence history with V limiter.

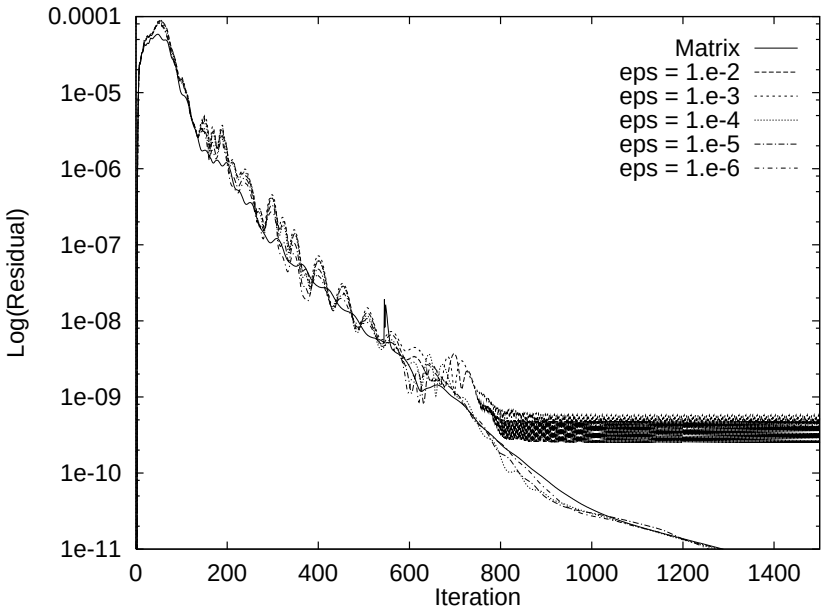

(b) Convergence history with Z limiter.

Figure B.6: Convergence history for ε study for Case 3.

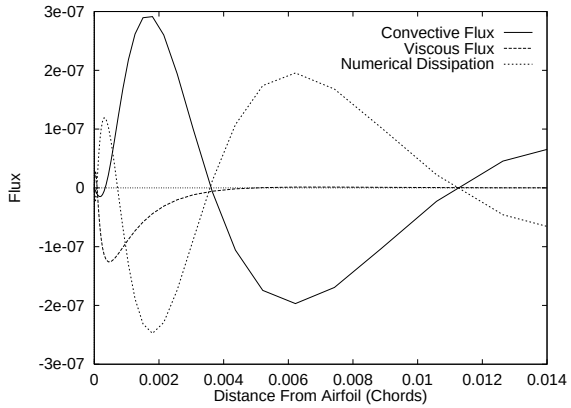

(a) Scalar Dissipation

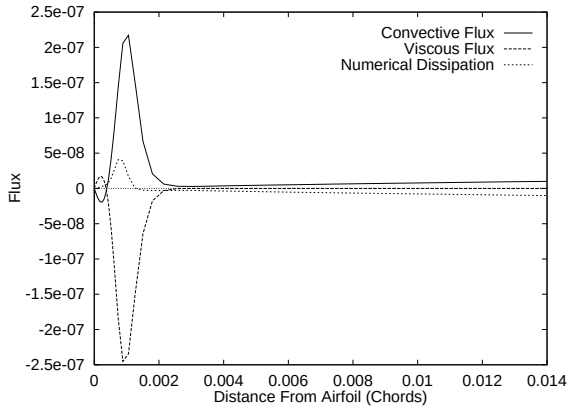

(b) Matrix Dissipation

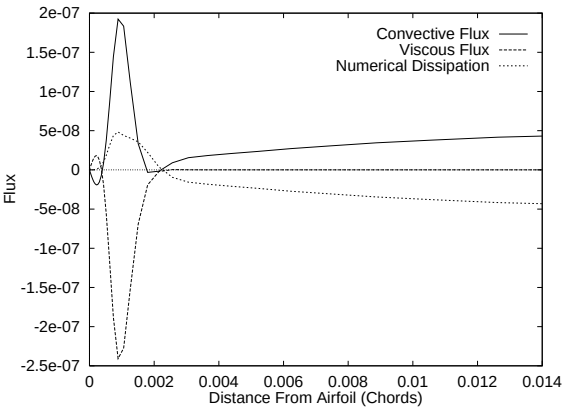

(c) CUSP Dissipation

Figure B.7: Flux balance for Case 1 on Grid B at 24% chord.

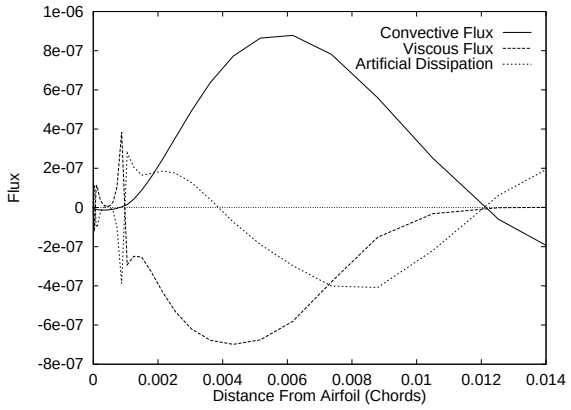

(a) Scalar Dissipation

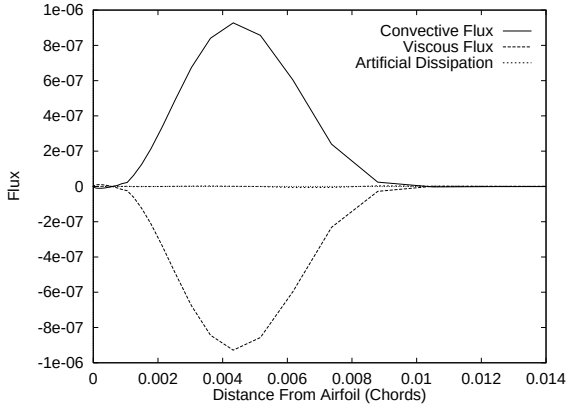

(b) Matrix Dissipation

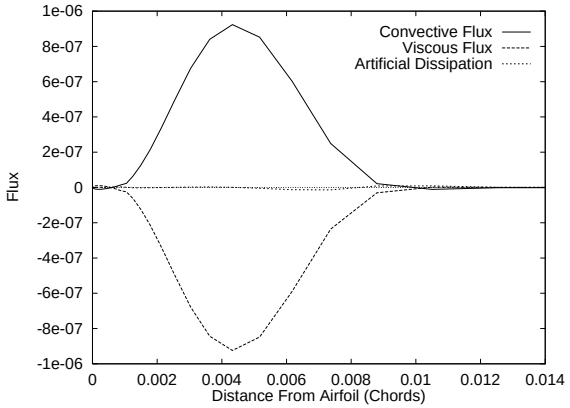

(c) CUSP Dissipation

Figure B.8: Flux balance for Case 1 on Grid B at 60% chord.

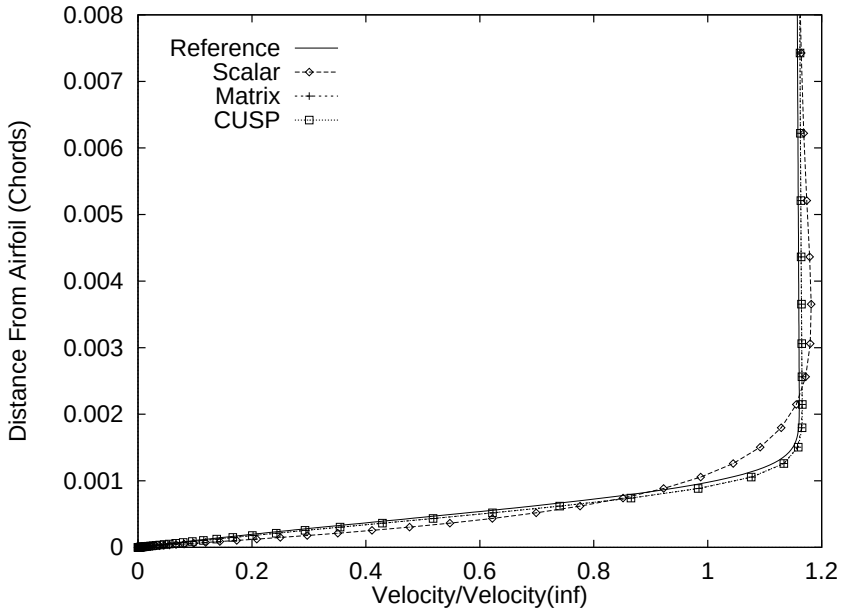

(a) 24% Chord

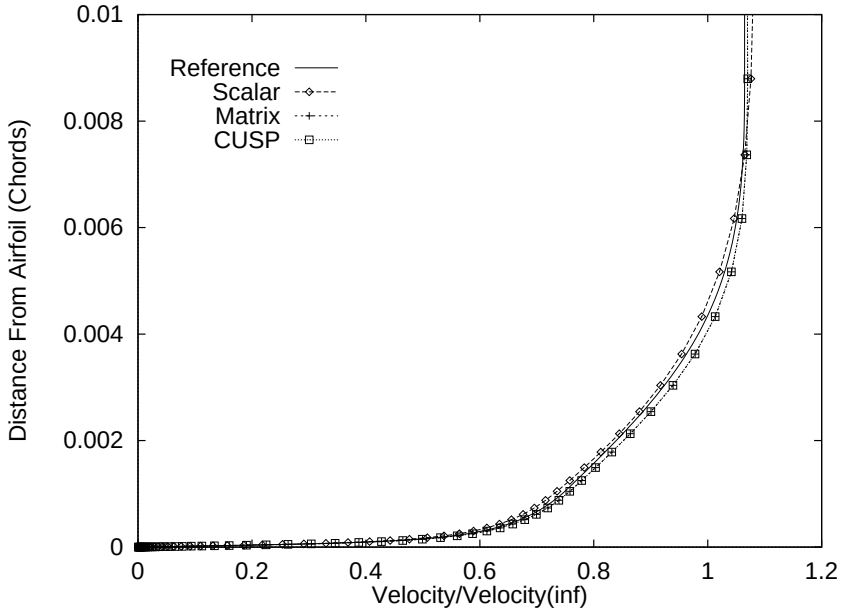

(b) 60% Chord

Figure B.9: Boundary layer profile for Case 1: NACA 0012 at $M_\infty = 0.16$ and $\alpha = 0°$.

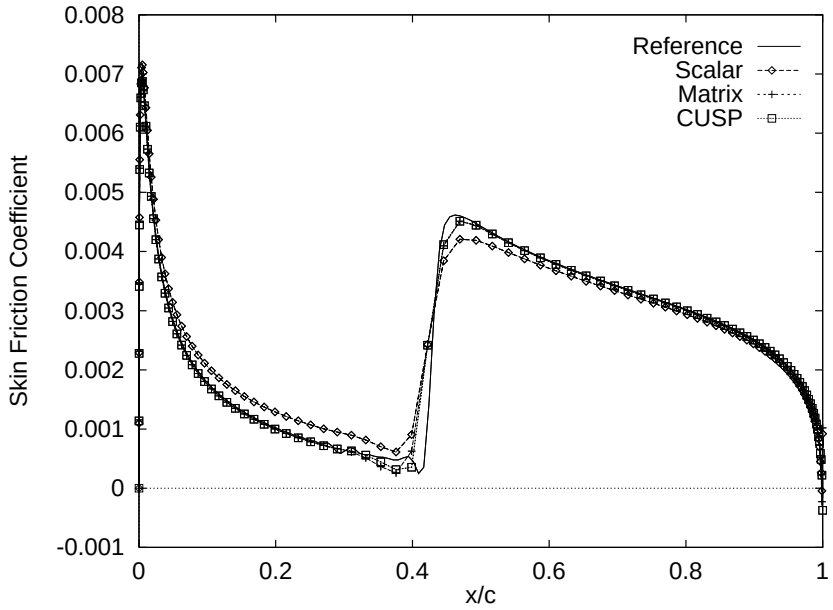

(a) Grid B (249×97)

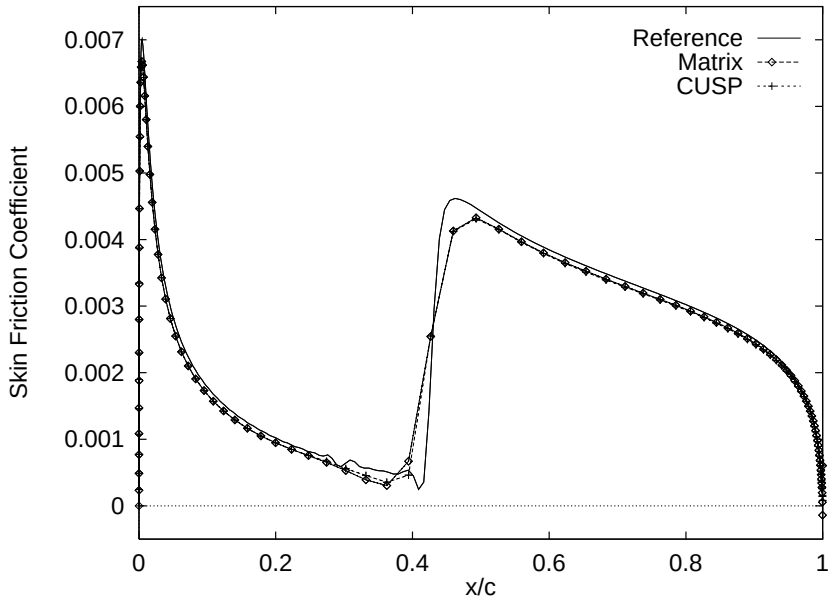

(b) Grid D (249×49)

Figure B.10: Skin friction coefficient for Case 1: NACA 0012 at $M_\infty = 0.16$ and $\alpha = 0°$.

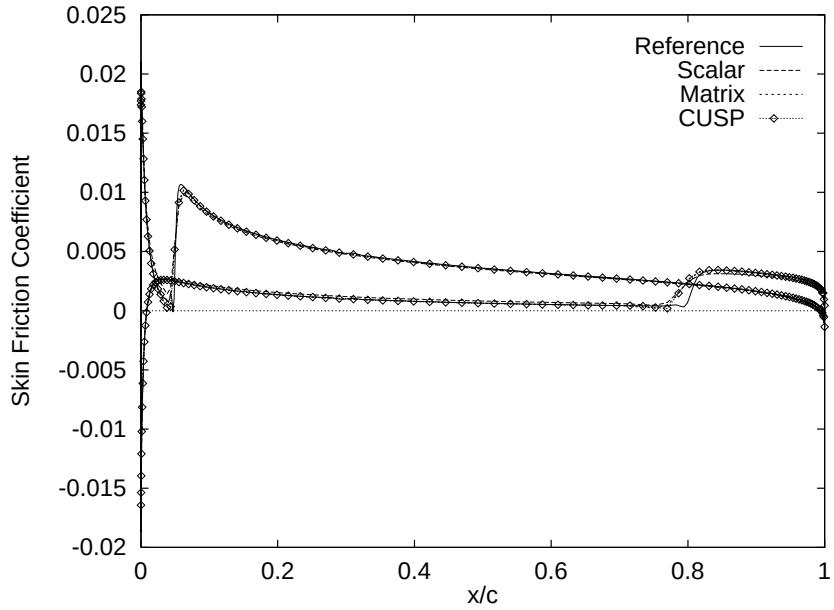

(a) Grid B (249×97)

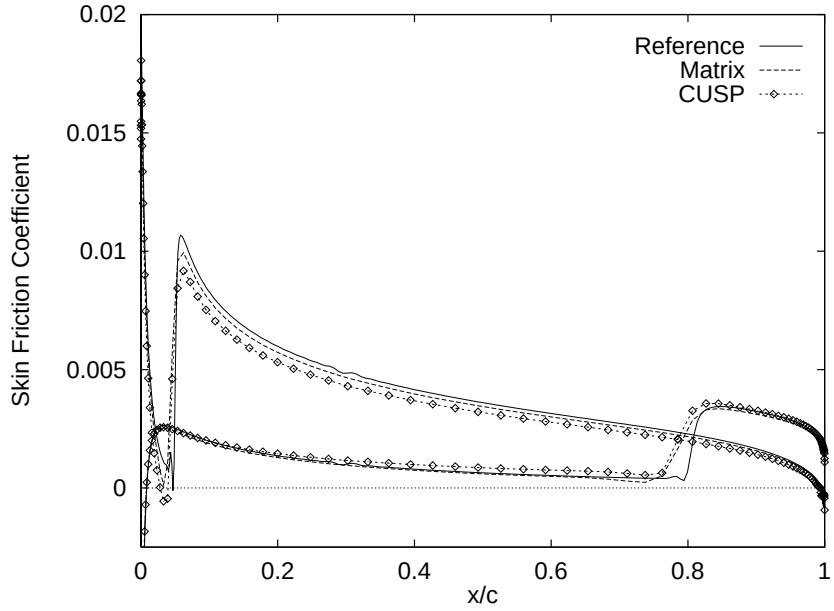

(b) Close-up of positive values for Grid D (249×49).

Figure B.11: Skin friction coefficient for Case 2: NACA 0012 at $M_\infty = 0.16$ and $\alpha = 6°$.

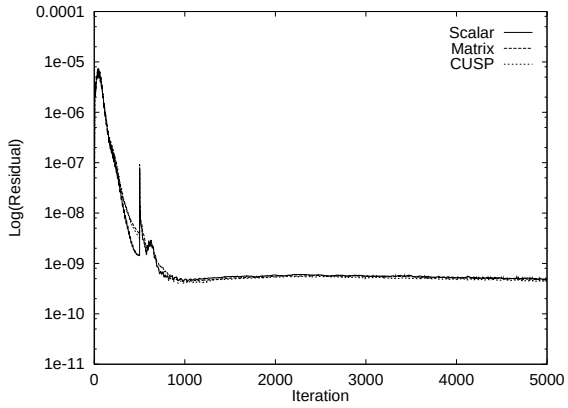

(a) Grid A (497×193)

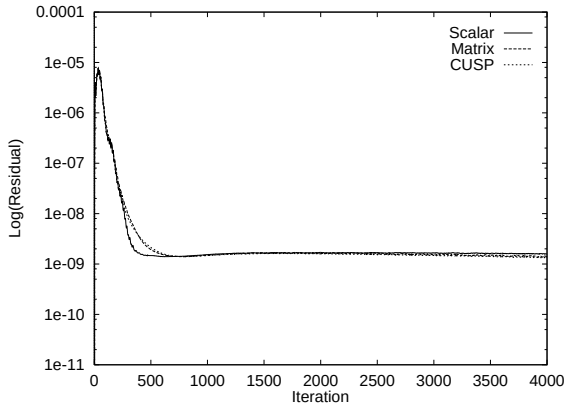

(b) Grid B (249×97)

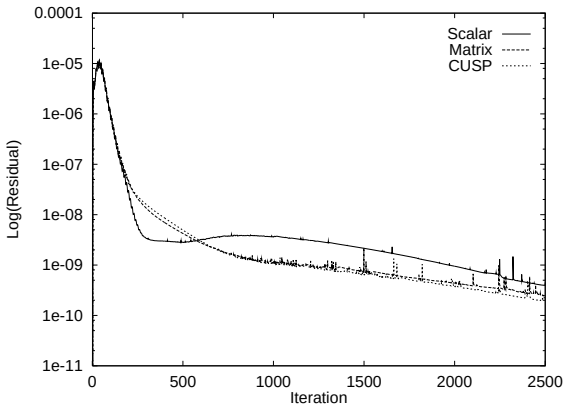

(c) Grid D (249×49)

Figure B.12: Convergence histories for Case 1: NACA 0012 at $M_\infty = 0.16$ and $\alpha = 0°$.

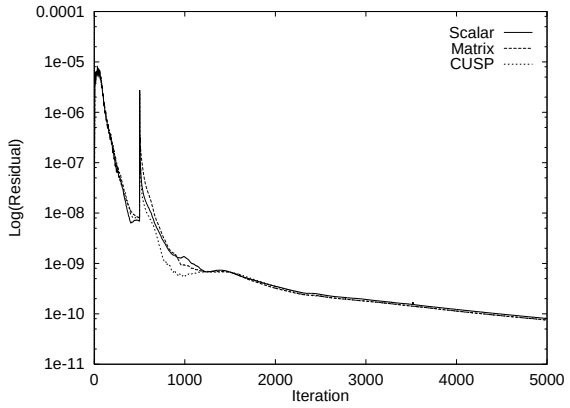

(a) Grid A (497×193)

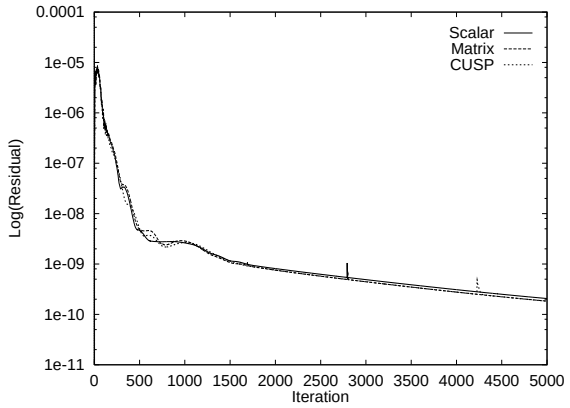

(b) Grid B (249×97)

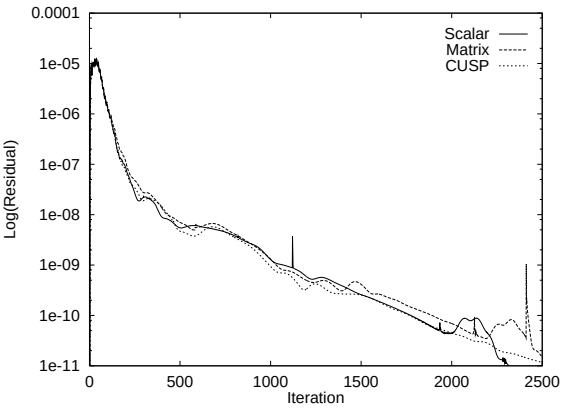

(c) Grid D (249×49)

Figure B.13: Convergence histories for Case 2: NACA 0012 at $M_\infty = 0.16$ and $\alpha = 6°$.

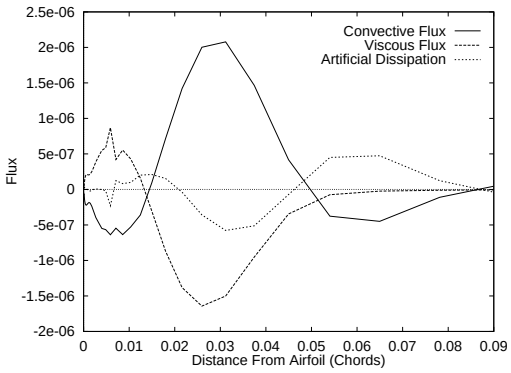

(a) Scalar Dissipation

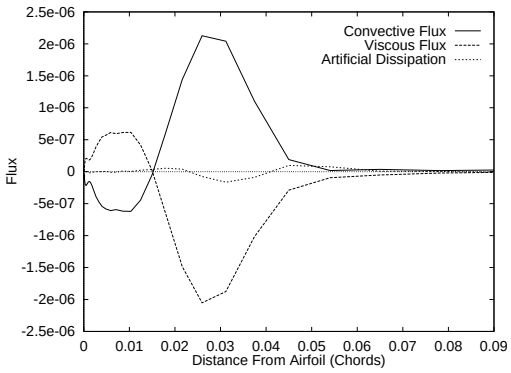

(b) Matrix Dissipation

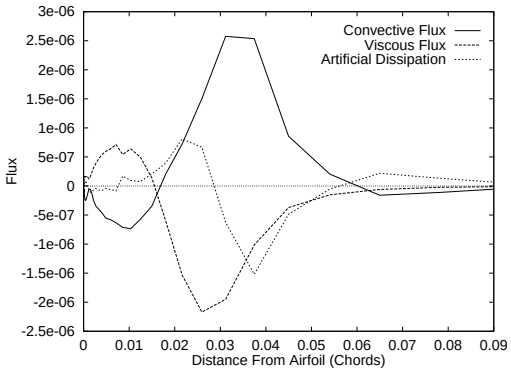

(c) CUSP V Limiter

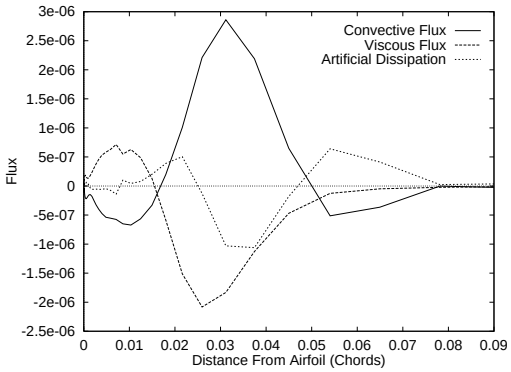

(d) CUSP Z Limiter

Figure B.14: Flux balance for Case 3 on grid C at 98 % chord.

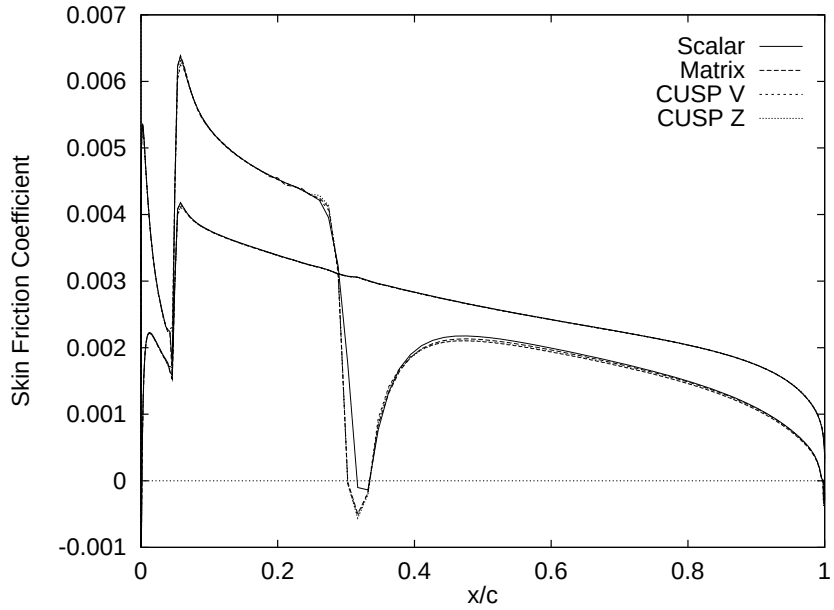

(a) Grid A (497×193)

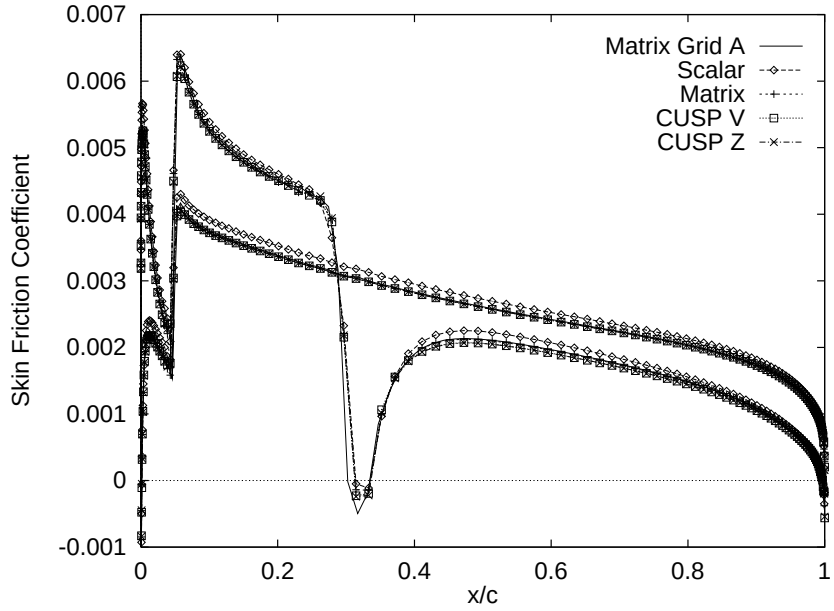

(b) Grid C (321×75)G

Figure B.15: C_{d_f} for Case 3: NACA 0012 at $M_\infty = 0.7$ and $\alpha = 3°$.

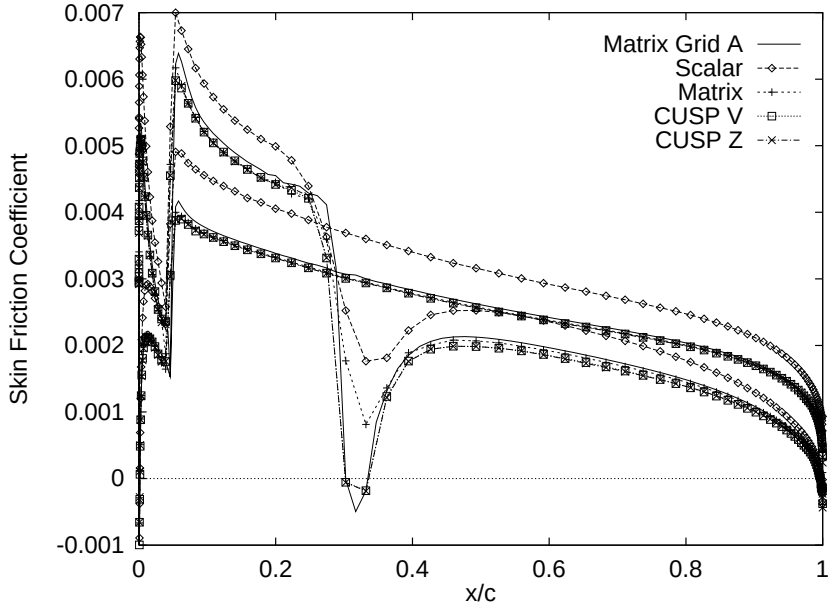

Figure B.16: C_{d_f} on grid D (249×49) for Case 3 (transition at 0.05 chords).

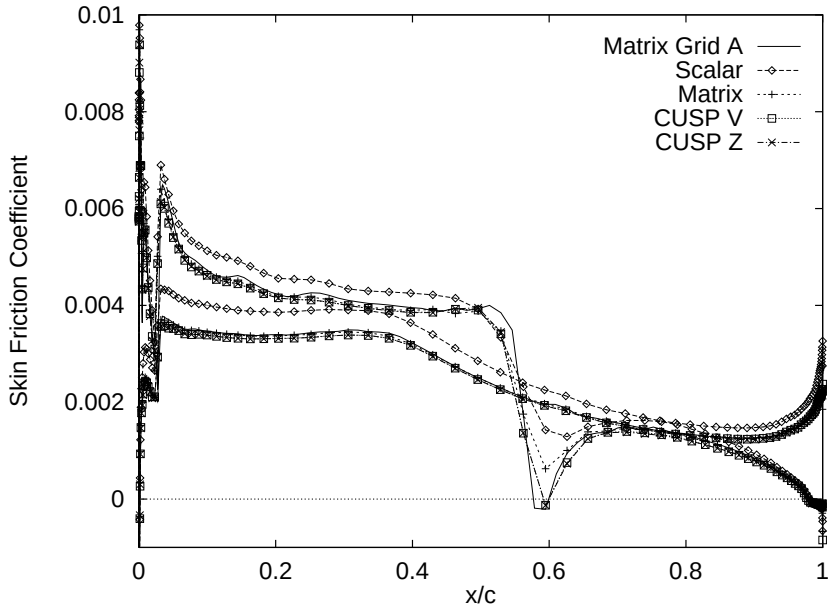

Figure B.17: C_{d_f} on grid D compared to grid A for Case 4 (transition at 0.03 chords).

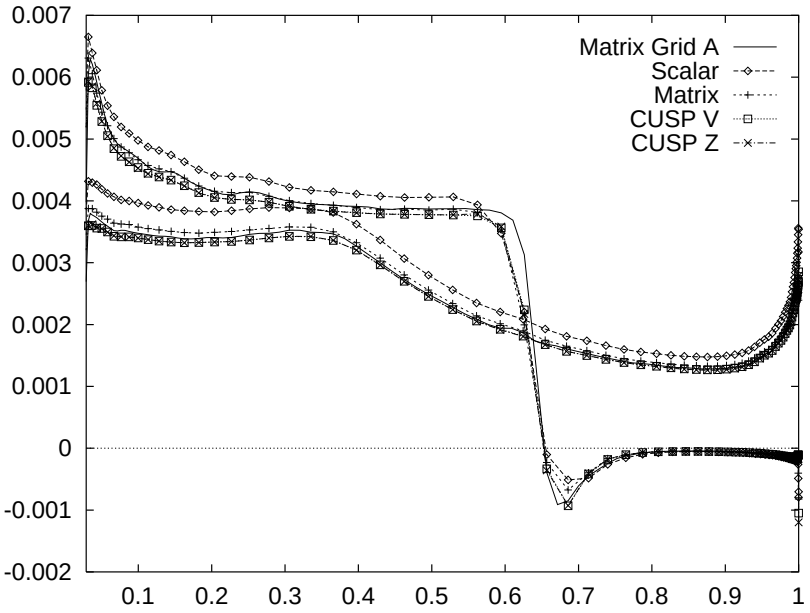

Figure B.18: C_{d_f} on grid D compared to grid A for Case 5 (turbulent region shown).

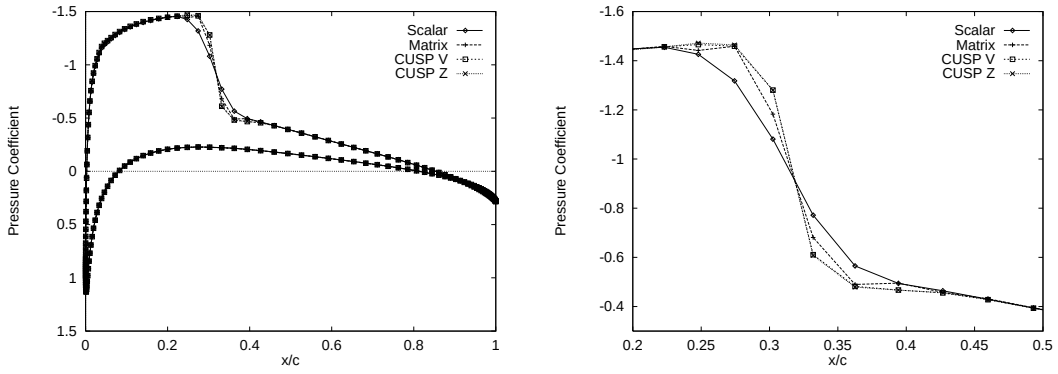

(a) C_p

(b) Close-up of shock region.

Figure B.19: C_p on grid D for Case 3: NACA 0012 at $M_\infty = 0.7$ and $\alpha = 3^\circ$.

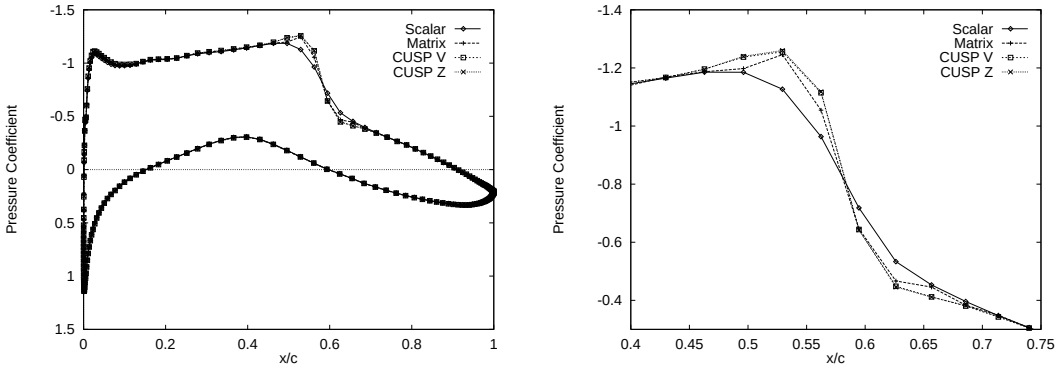

(a) C_p (b) Close-up of shock region.

Figure B.20: C_p on grid D for Case 4: RAE 2822 at $M_\infty = 0.729$ and $\alpha = 2.31°$.

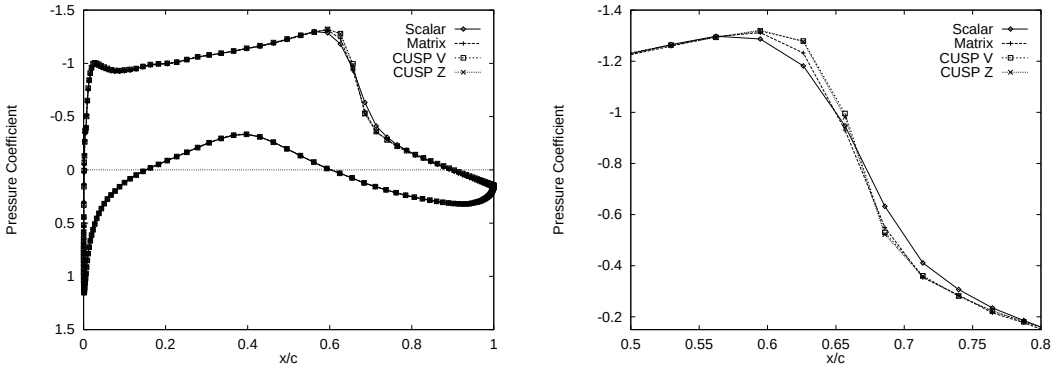

(a) C_p (b) Close-up of shock region.

Figure B.21: C_p on grid D for Case 5: RAE 2822 at $M_\infty = 0.754$ and $\alpha = 2.57°$.

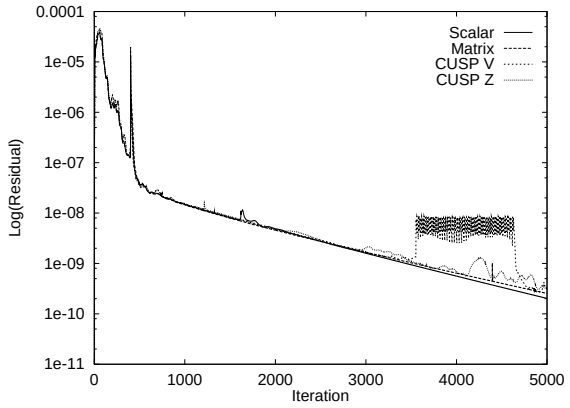

(a) Grid A (497×193)

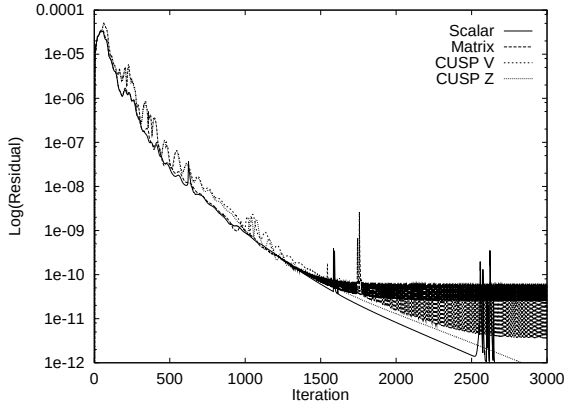

(b) Grid C (321×75)

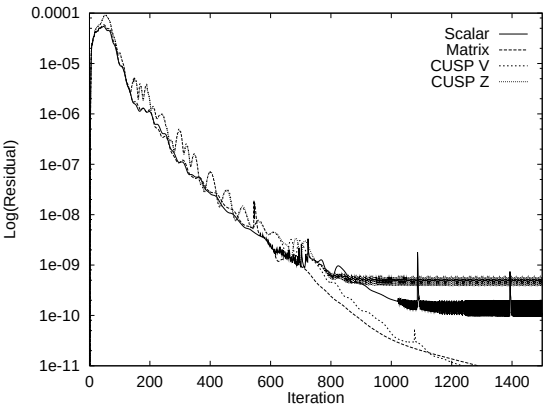

(c) Grid D (249×49)

Figure B.22: Convergence histories for Case 3: NACA 0012 at $M_\infty = 0.7$ and $\alpha = 3°$.

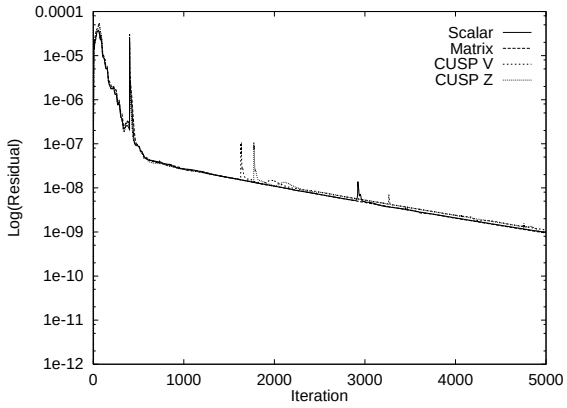

(a) Grid A (497×193)

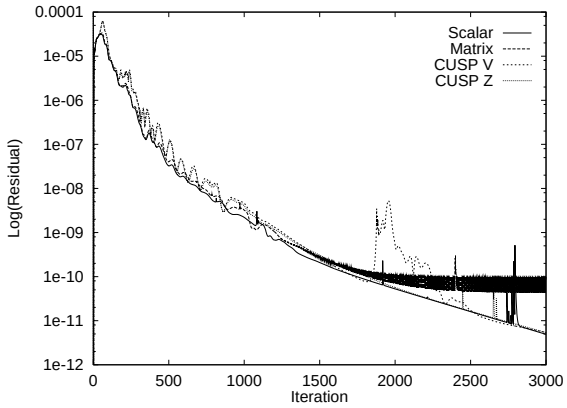

(b) Grid C (321×75)

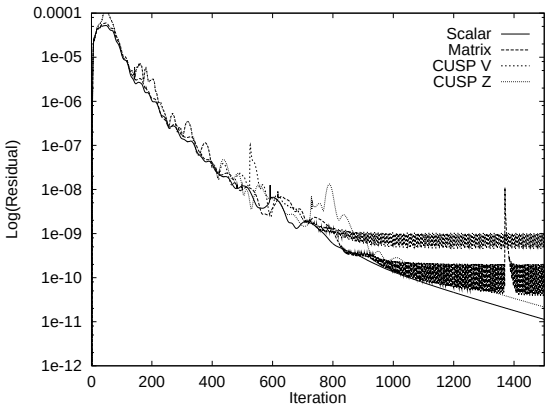

(c) Grid D (249×49)

Figure B.23: Convergence histories for Case 4: RAE 2822 at $M_\infty = 0.729$ and $\alpha = 2.31°$.

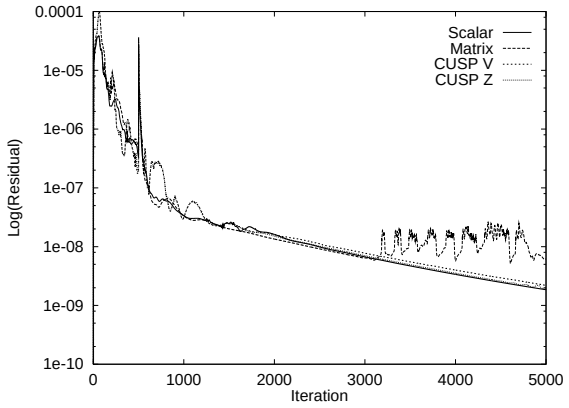

(a) Grid A (497×193)

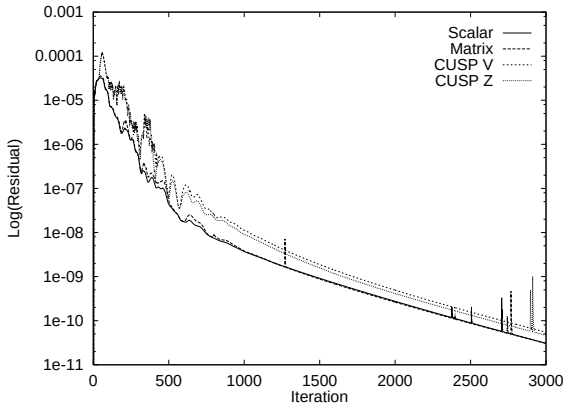

(b) Grid C (321×75)

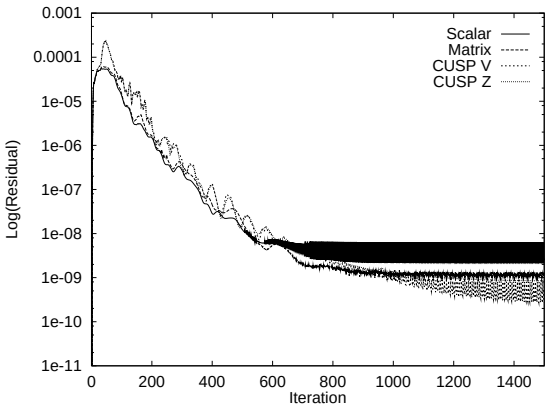

(c) Grid D (249×49)

Figure B.24: Convergence histories for Case 5: RAE 2822 at $M_\infty = 0.754$ and $\alpha = 2.57°$.

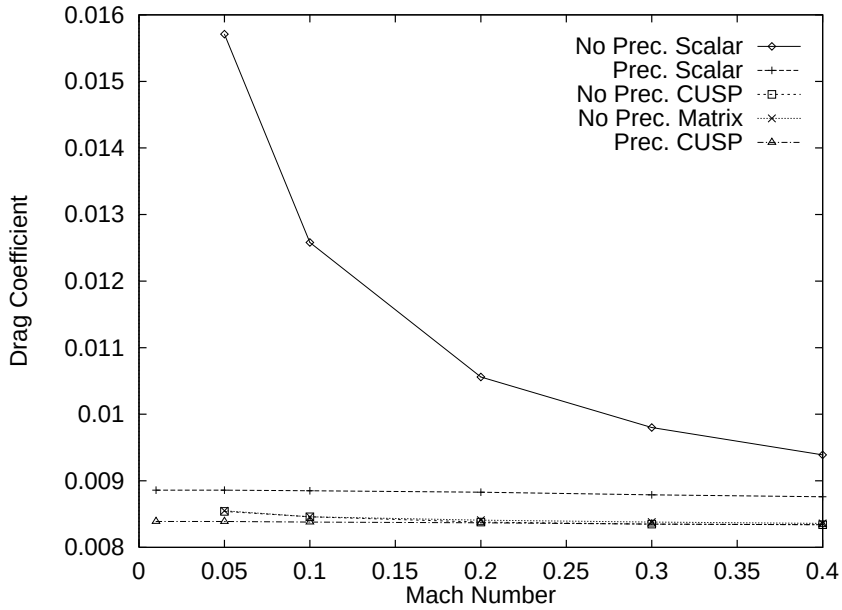

(a) C_d

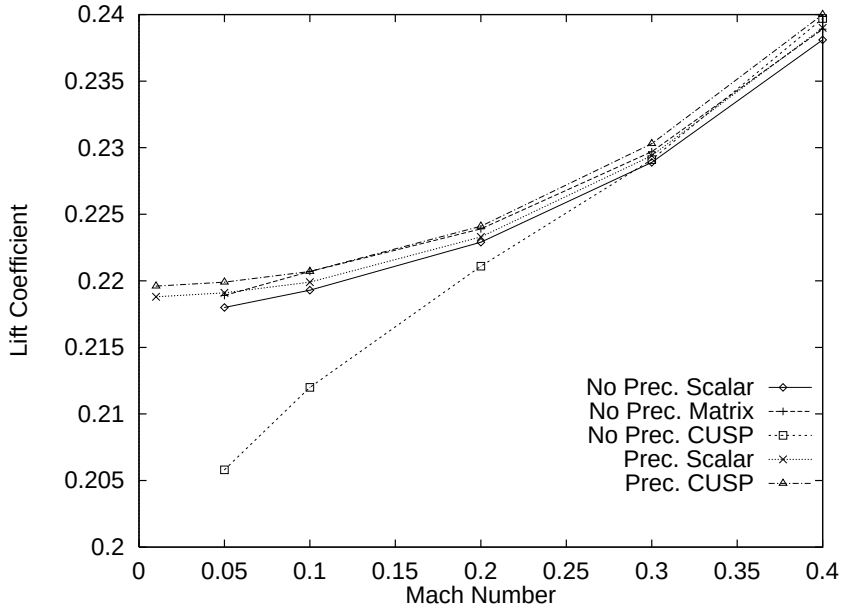

(b) C_l

Figure B.25: Variation of drag and lift as a function of M_∞ for $\alpha = 2^\circ$.

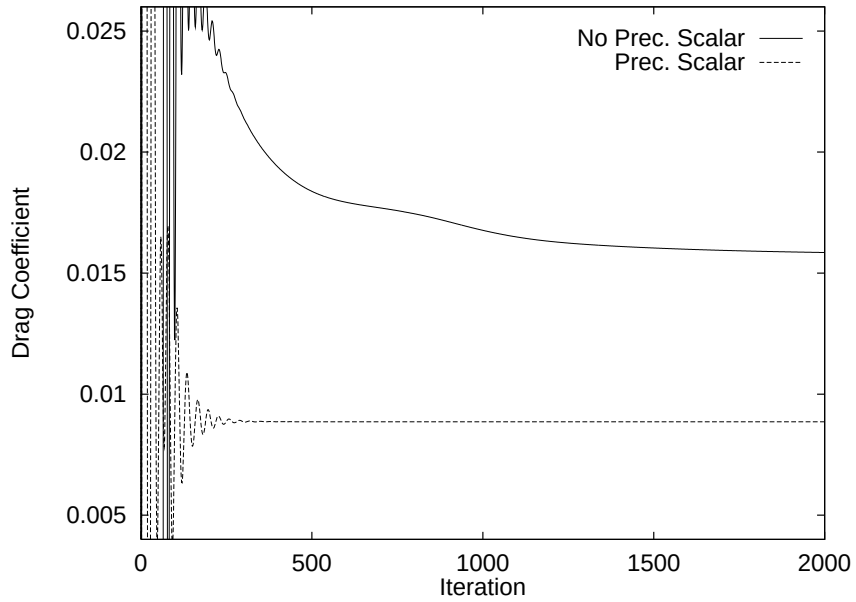

(a) C_d with scalar dissipation.

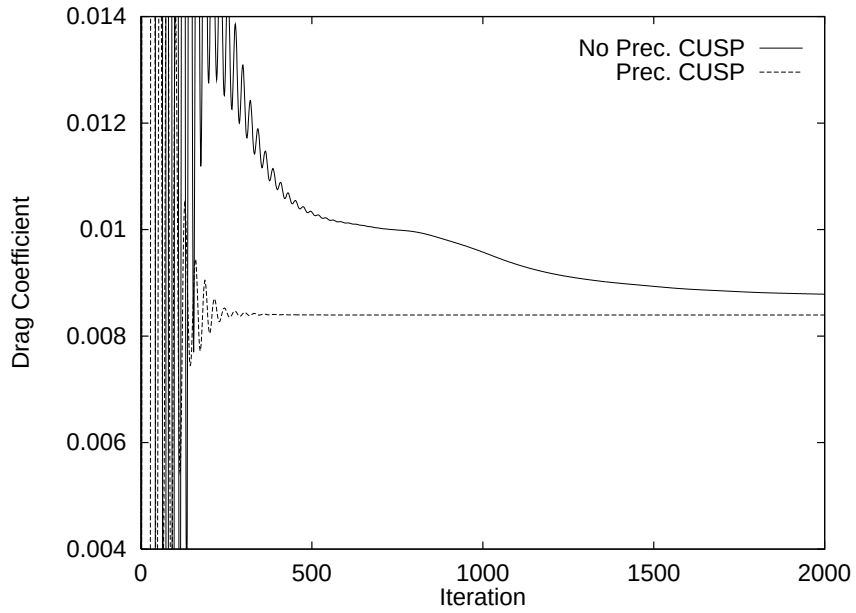

(b) C_d with CUSP dissipation.

Figure B.26: Convergence of drag for $M_\infty = 0.05$ and $\alpha = 2°$.

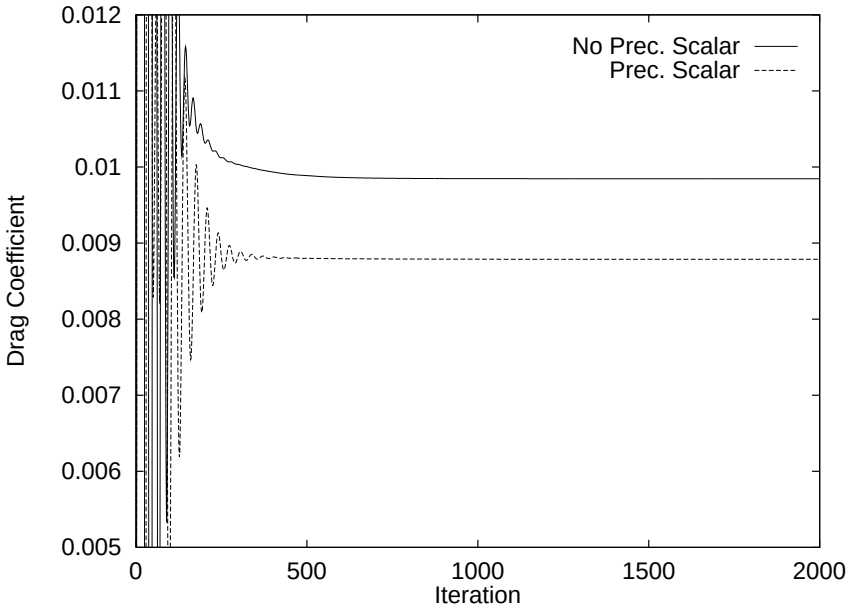

(a) C_d with scalar dissipation.

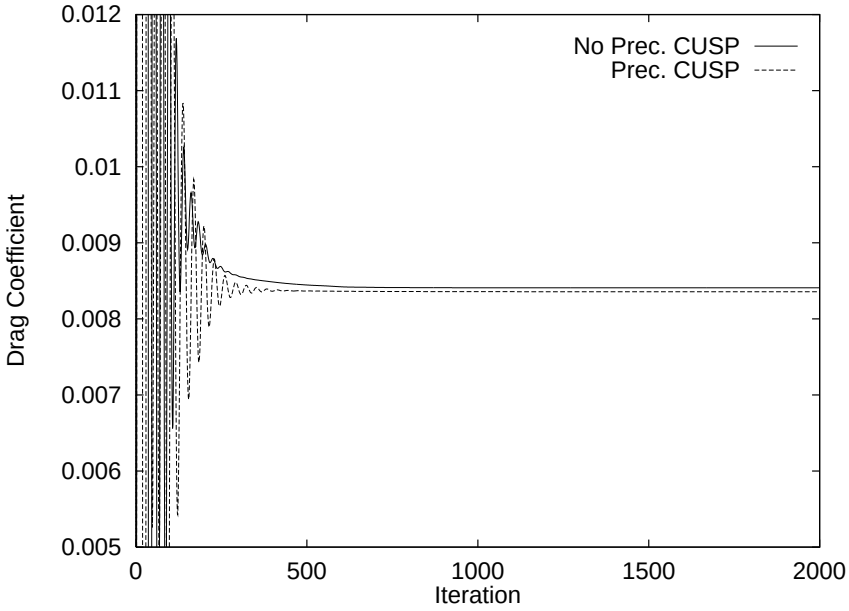

(b) C_d with CUSP dissipation.

Figure B.27: Convergence of drag for $M_\infty = 0.3$ and $\alpha = 2^\circ$.

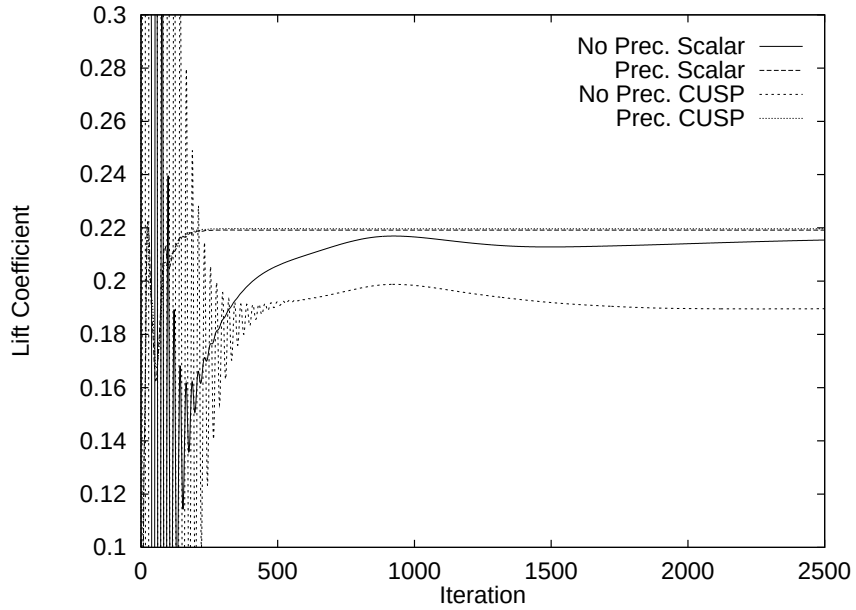

(a) C_l convergence.

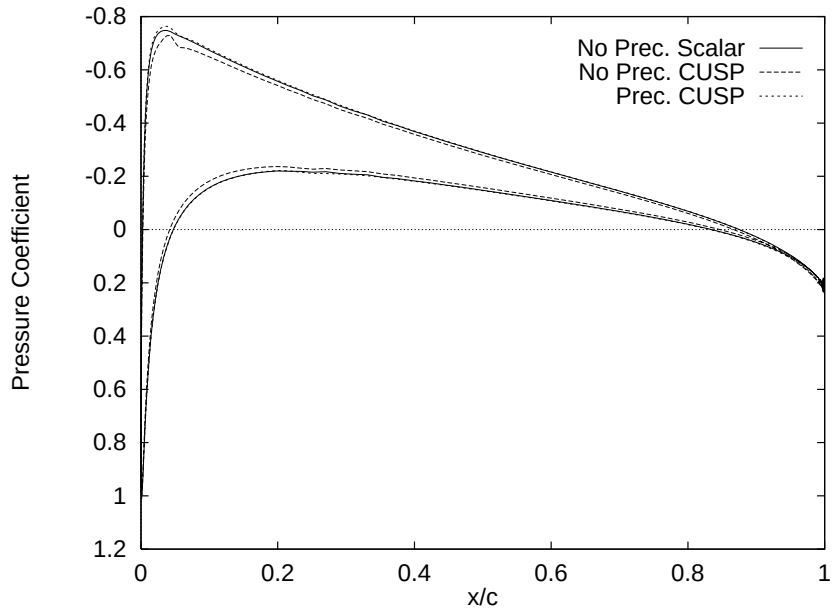

(b) C_p distribution.

Figure B.28: Convergence of lift for $M_\infty = 0.05$ and $\alpha = 2°$.

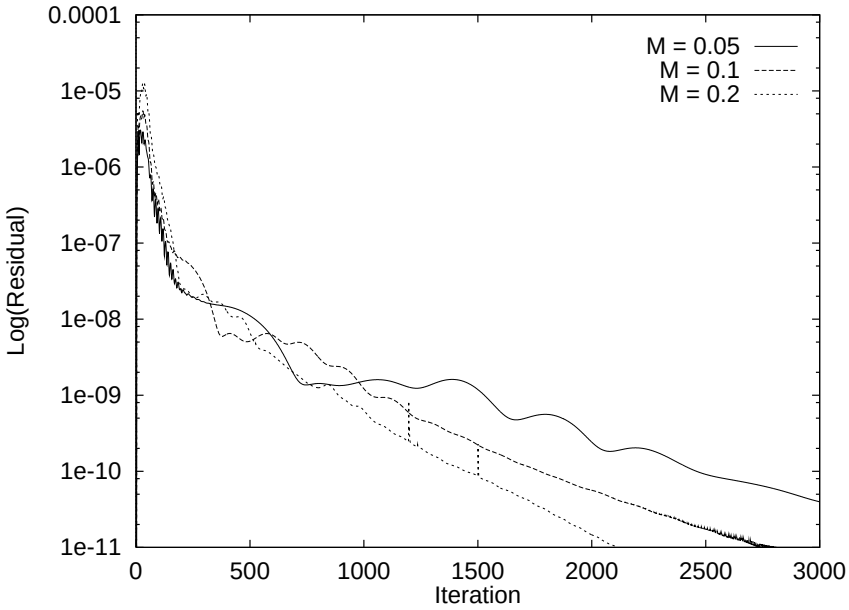

(a) Scalar dissipation without preconditioning.

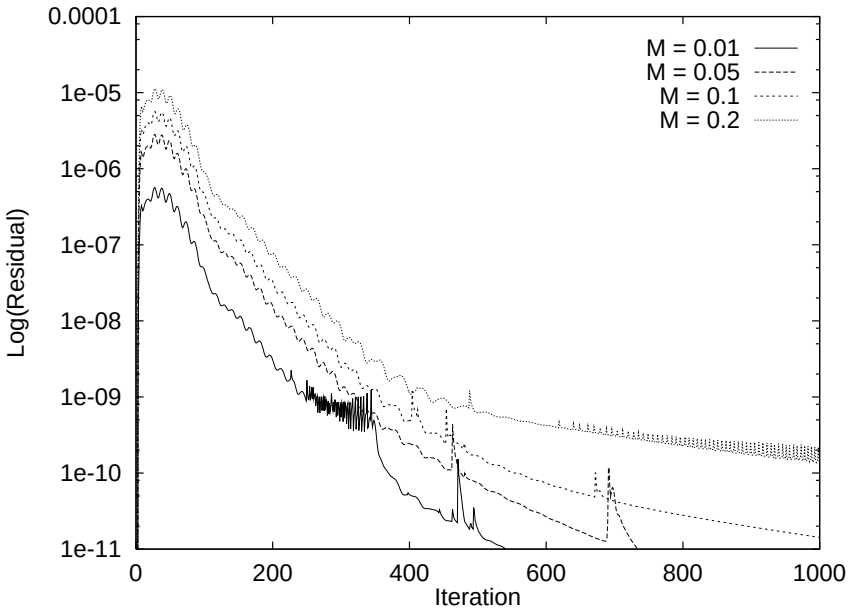

(b) Scalar dissipation with preconditioning.

Figure B.29: Convergence histories for scalar dissipation.

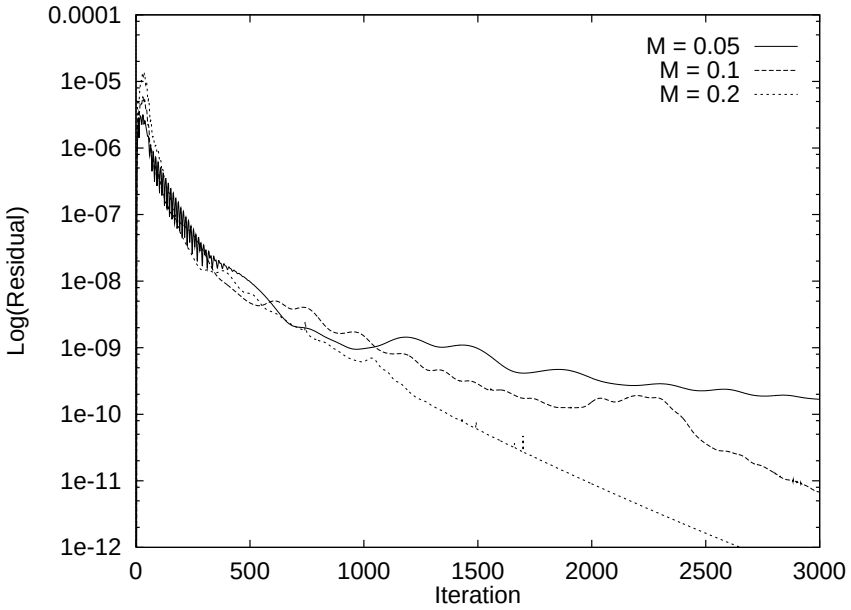

(a) CUSP dissipation without preconditioning.

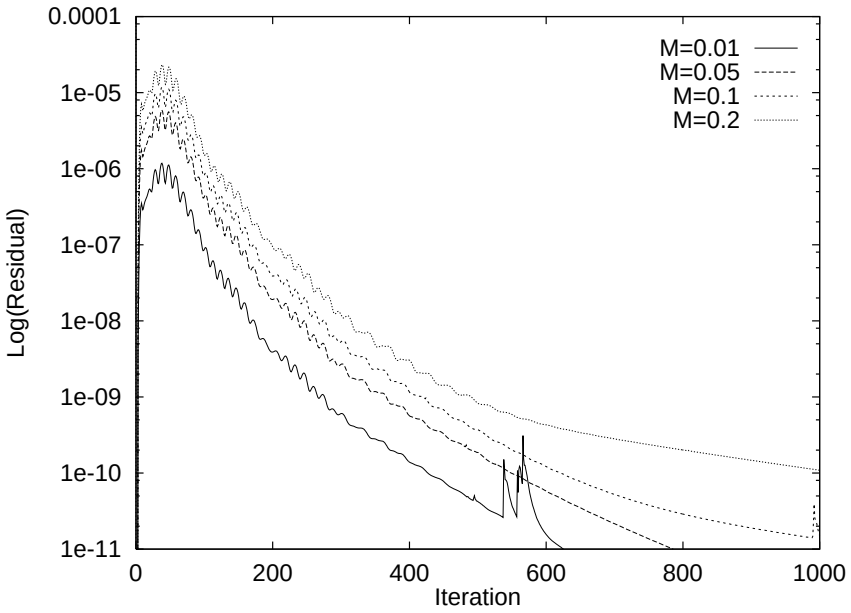

(b) CUSP dissipation with preconditioning.

Figure B.30: Convergence histories for CUSP dissipation.

Appendix C

Notes on Implementation

The following changes were made to SC1 in order to implement the CUSP scheme:

1. On the RHS, three subroutines were added to *xiexpl.f* and *etaexpl.f* respectively. These subroutines are *dclimx.f*, *dclimy.f*, *dcexpx.f*, *dcexpy.f*, *dcexpx2.f*, and *dcexpy2.f*.

2. On the LHS, the subroutines *stepf2dx.f* and *stepf2dy.f* were modified to include the eigenvalues of the CUSP scheme.

The user flag 'LIMITER' must be set in the input file to select a limiter as follows: LIMITER=1 corresponds to third-order dissipation, LIMITER=2 corresponds to first-order dissipation, LIMITER=3 corresponds to the Z limiter, LIMITER=4 corresponds to the V limiter, and LIMITER=5 corresponds to limiter freezing. When freezing the limiter, it is necessary to specify the number of iterations for which the limiter is active in subroutines *dclimx.f* and *dclimy.f*. When the Z or V limiters are used, the variables EPZ and EPV should be set to the desired value of ε. The input parameter DCUSP4 corresponds to the parameter κ_4 which is normally set to a value of 1.0.

The CUSP scheme is implemented to work with the following options:

- CMESH=FALSE
- PERIODIC=FALSE
- BCAIRF=TRUE
- ITMODEL=1
- METH=3